

Final Report

**ADVANCED OPTICAL AND ELECTROSTATIC
CHARACTERIZATION OF CLOSED-ELECTRON
DRIFT THRUSTERS**

Prepared by:

Professor Mark A. Cappelli, Principal Investigator
Mechanical Engineering Department
Stanford University
Stanford, California 94305-3032
Tel: (650) 725-2020, Fax: (650) 723-1748, email: cap@leland.stanford.edu

Prepared for:

Dr. Mitat Birkan

DISTRIBUTION STATEMENT A
Approved for Public Release
Distribution Unlimited

Under AFOSR Grant No: F49620-97-1-0372

HIGH TEMPERATURE GASDYNAMICS LABORATORY
Mechanical Engineering Department
Stanford University

REPORT DOCUMENTATION PAGE

Public reporting burden for this collection of information is estimated to average 1 hour per response, including gathering and maintaining the data needed, and completing and reviewing the collection of information. Send comments regarding this burden estimate or any other aspect of this collection of information, including suggestions for reducing this burden, to Washington Headquarters Service, Paperwork Project, Suite 1204, Arlington, VA 22202-4302, and to the Office of Management and Budget, Paperwork Project, Suite 1204, Arlington, VA 22202-4302.

AFRL-SR-BL-TR-01-

Source,
of this
Person

0290

1. AGENCY USE ONLY (Leave blank)		2. REPORT DATE 18 Apr 01	3. RE FINAL REPORT 01 Jun 97 TO 31 Aug 00
4. TITLE AND SUBTITLE ADVANCED OPTICAL AND ELECTROSTATIC CHARACTERIZATION OF CLOSED-ELECTRON DRIFT THRUSTERS			5. FUNDING NUMBERS F49620-97-1-0372
6. AUTHOR(S) Prof. Mark A. Cappelli			
7. PERFORMING ORGANIZATION NAME(S) AND ADDRESS(ES) Mechanical Engineering Department Stanford University Stanford California 94305-3032			8. PERFORMING ORGANIZATION REPORT NUMBER
9. SPONSORING/MONITORING AGENCY NAME(S) AND ADDRESS(ES) AFOSR/NA 801 N. Randolph St. Arlington VA 22203			10. SPONSORING/MONITORING AGENCY REPORT NUMBER
11. SUPPLEMENTARY NOTES			
12a. DISTRIBUTION AVAILABILITY STATEMENT Approve for public release.			12b. DISTRIBUTION CODE
13. ABSTRACT (Maximum 200 words) The research funded under this grant has been extremely successful, providing partial support for two graduate students (Mr. D. Schmidt, and Mr. Q. Walker). Over the course of the three years, these two students funded under this augmentation grant have published a total of three archival papers, and ten conference papers (see Publication Section). Here we provide a brief description of the research and results obtained to date, and direct the reader to the extensive publication list, where the findings are described in considerable detail. In some cases, papers are provided as attachments in the Appendix.			
14. SUBJECT TERMS Advanced Optical and Electrostatic Characterization			15. NUMBER OF PAGES
			16. PRICE CODE
17. SECURITY CLASSIFICATION OF REPORT UNCLASSIFIED	18. SECURITY CLASSIFICATION OF THIS PAGE UNCLASSIFIED	19. SECURITY CLASSIFICATION OF ABSTRACT UNCLASSIFIED	20. LIMITATION OF ABSTRACT UL

Final Report

**ADVANCED OPTICAL AND ELECTROSTATIC
CHARACTERIZATION OF CLOSED-ELECTRON
DRIFT THRUSTERS**

Prepared by:

Professor Mark A. Cappelli, Principal Investigator
Mechanical Engineering Department
Stanford University
Stanford, California 94305-3032
Tel: (650) 725-2020, Fax: (650) 723-1748, email: cap@leland.stanford.edu

Prepared for:

Dr. Mitat Birkan

Under AFOSR Grant No: F49620-97-1-0372

Final Report

ADVANCED OPTICAL AND ELECTROSTATIC CHARACTERIZATION OF CLOSED-ELECTRON DRIFT THRUSTERS

Grant No: F49620-97-1-0372

Mark A. Cappelli

Mechanical Engineering Department

Stanford University

Stanford, California 94305-3032

Tel: (650) 725-2020, Fax: (650) 723-1748, email: cap@leland.stanford.edu

Executive Summary

Motivation There is an increasing need to develop diagnostics (both non-intrusive laser-based diagnostics, and electrostatic probe diagnostics) to better understand the complex time-average and also the unsteady phenomenon occurring in novel plasma propulsion devices. Under this grant, we have provided support for graduate students to further develop appropriate diagnostic methods for a new, novel linear Hall plasma source that shows much promise to operate in regimes (ultra low power - < 100 W) not yet successfully covered with similar discharges of co-axial geometries. Also, we have developed electrostatic probe techniques to monitor the propagation of instabilities in the broader range of Hall discharge types. The motivation for these probe studies is to improve our understanding of how fluctuations control electron flow in Hall thrusters, and how such knowledge can lead to insight as to why a linear geometry thruster (with an open electron drift) should work (and work well). Finally, we have developed and applied new laser-induced fluorescence methods to probe arc-heated He jets, which we propose to use as neutralizing cathodes for Hall thruster clusters. Such clusters are presently being considered by the Air Force for use in very high thrust and power regimes. The combination of an arcjet cathode and a cluster of Hall discharge anodes is shown to lead to a hybrid concept that has an operating envelope that lies in-between that of a high power arcjet, and a high power (conventional) Hall discharge.

Accomplishments The research funded under this grant has been extremely successful, providing partial support for two graduate students (Mr. D. Schmidt, and Mr. Q. Walker). Over the course of the three years, these two students funded under this augmentation grant have published a total of three archival papers, and ten conference papers (see Publications Section). Here we provide a brief description of the research and results obtained to date, and direct the reader to the extensive publication list, where the findings are described in considerable detail. In some cases, papers are provided as attachments in the Appendix.

Linear Hall Thruster Laser-Induced Fluorescence Measurements

It has been an objective of the core AFOSR-funded program, to understand the physics of these devices, so as to be able to scale the thrusters down to very low power levels. The operation of $E \times B$ discharge accelerators at these low power ranges introduces many engineering challenges. These include increased heat loads imposed on the structure due to the nature of the scaling of these plasma devices, and the increased frequency (possibly into the MHz regime, also due to the nature of the scaling) of the strong "loop" instabilities and its impact on the plasma, and power processing unit, amongst others. At Stanford, we have developed and tested a linear-geometry, open electron drift

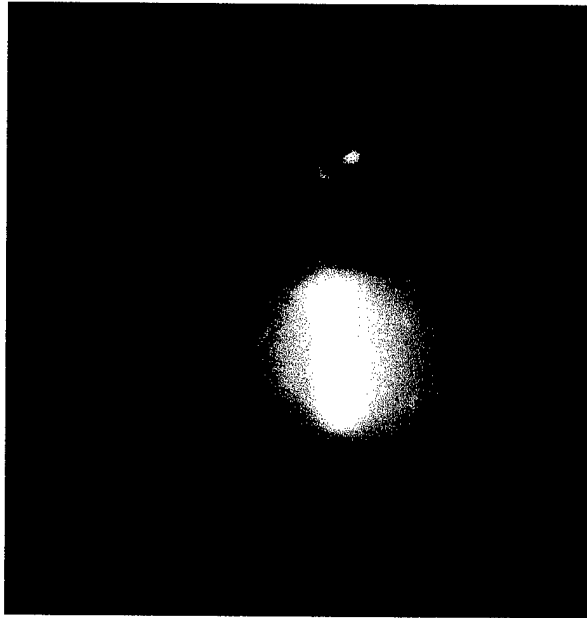


FIG. 1. Photograph of linear thruster operating at about 75W of discharge power.

Hall discharge (see Appendix I). The linear geometry makes it feasible to use permanent magnets instead of electromagnets (this is important if micro-fabrication methods are to be introduced). The impetus for a linear geometry was largely the result of the experiments described above on co-axial geometries, which indicate that the drifting electrons may not make a complete revolution around the thruster before traversing the region of strong magnetic fields.

A photograph of the linear-geometry thruster that we (initially lead by D. Schmidt under the ASSERT grant) have fabricated and tested while operating at about 75W of power is shown in Fig. 1. Details of the geometry and operating characteristics have been previously published (Ref. 1, and Publications 1, 6, see also Appendix I], although we have not yet published any details on the performance, which is quite encouraging. Using facilities down at Edwards

Air Force Base, we were able to characterize the performance of this linear thruster over a wide range of conditions. The thrust efficiency is found to exhibit a significant increase with decreasing power, unlike the behavior seen in coaxial devices. At the low power operating point, where the efficiency exceeded 14%, the measured specific impulse approached 1100 seconds. As far as we know, no other ultra-low power Hall discharge has performed so well at these conditions, despite the lack of design optimization. As part of the ASSERT project, Q. Walker further examined the performance of this linear-geometry thruster by LIF diagnostics to measure the ion velocity along the channel and downstream of the thruster. The results of this study show that ions are leaving the channel at high velocity and are accelerating as they leave the channel, in a manner that is consistent with what was measured on the thrust stand down at Edwards AFB.

For the LIF diagnostics, the $5d[4]_{7/2} - 6p[3]_{5/2}$ ion transition at 834.7 nm was chosen for this study based on our previous experience with ion velocity measurements with Hall thrusters. Since the isotopic and nuclear spin splitting constants of this transition are not fully known, the ion temperature cannot be measured. An advantage of using the line is the ability to do non-resonant fluorescence collection. The strong line at 541.9 nm that emanates from the same upper state is used to collect fluorescence. A Coherent 899-21 Ti: Sapphire Ring laser pumped by a Coherent Verdi 5-W Nd:YAG produces laser radiation at 834.7 nm. The laser wavelength is monitored with a Burleigh Instruments WA-1000 scanning Michaelson interferometer wavemeter. This probe beam is focused into the plume of the linear Hall thruster, and the fluorescence is collected at a right angle to the excitation. The collected light is focused onto the entrance slit of a monochromator, which is used as a narrow band filter for the 541.9 nm transition. The only difference between this setup and the setup used for previous LIF studies in co-axial thrusters by our group is the scan time needed to collect the LIF signal. The LIF signal is much stronger with the linear thruster and as a result a shorter integration time and scan time is needed to capture the lineshape. The strong signal also made it difficult to obtain lineshapes that are not broadened due to the laser intensity. Even with lower laser intensities and properly adjusting the integrations and scan time, the lineshapes remained

Cathode	Anode	Anode Voltage	Anode Current	Magnet
3 sccm	2 sccm	100.49 – 100.67 V	0.45 – 0.40 A	0.25 A
1 sccm	2 sccm	100.69 – 100.92 V	0.21 – 0.17 A	0.25 A

Table 1. Linear Hall Thruster Operating Conditions

a slightly lower power than those for which we have thrust measurements. For these studies, the linear thruster used the boron nitride acceleration channel. Fig. 2 shows the ion velocity profile at the exit plane for these conditions. These data were taken along the centerline of the 25 mm long channel. These velocities are comparable to those we measured at the exit plane of a coaxial Hall thruster. This confirms that the linear Hall thruster is producing thrust. As expected, with a greater power, the ions experience a greater acceleration. Both profiles also show a greater velocity near the top of the channel where the cathode is located. This is the same direction as the crossed electric and magnetic field.

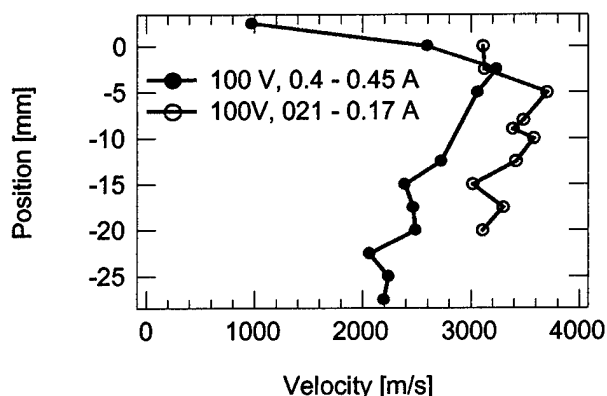


Fig. 2. Linear Hall Thruster Axial Exit Velocities at different operating conditions.

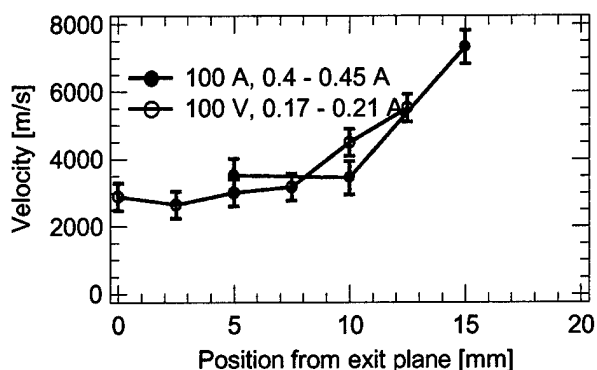


Fig. 3. Ion velocities downstream at 0.40A, 100.8 V

saturated. These saturated lineshapes are not problematic for measuring velocity, but further prohibit the accurate determination of the ion temperature.

Table 1 shows the operating conditions for the linear thruster, at which LIF studies were performed. These operating conditions are at

Fig. 3 shows the acceleration of the ions as they leave the thruster channel. The measurements were taken half way from the top of the channel, and the cathode plane is roughly 1 cm downstream from the thruster exit plane. There is evidence of acceleration before the cathode plane only for the low power level. In both cases, the ions continue to accelerate past the cathode plane. The lineshapes recorded further downstream show evidence of ions at multiple velocities. This suggests that the ion velocity distribution is no longer Maxwellian as has been observed in measurements on co-axial thrusters [2].

This study has demonstrated that the linear Hall thruster does accelerate ions along its channel and it is indeed producing thrust. Further studies will be conducted into improving the overall design of the linear Hall thruster. We are currently building a new thruster specifically designed for a more robust anode and magnetic circuit. The ion velocity measurements are just a small part of the ongoing characterization of the performance and operation of a low-power linear Hall thruster.

Measurements of Plasma Wave Propagation

Using extensive measurements of the time-averaged plasma properties in the discharge channel, including laser-induced fluorescence measurements of neutral and ionized xenon velocities [as supported under the core grant] graduate student D. Schmidt has fabricated and used various electrostatic probe diagnostics [Ref. 3, see also Publications 3, 7, 10, 12] and Appendix II] to map out time dependent plasma density fluctuations at frequencies $f < 400$ kHz, allowing us to extensively characterize the dynamical behavior of plasma density within the discharge channel. An example of a spectral map (frequency-position) depicting the local fluctuations in plasma density within the discharge channel is shown in Fig. 4.

A comparison (conditional cross-spectral analysis) of the signal from two Langmuir probes, located at the same axial position, but separated by some angle on the azimuth, was used to measure the azimuthal component of the phase velocity (wave dispersion). Fig. 5 shows a typical dispersion plot, rich in features, clearly showing the presence of four characteristic modes, the most prominent of which is that of a pure azimuthally propagating disturbance ($m=1$) with frequencies in the 5-20 kHz range, and of phase velocity $V_p \sim 1000 - 4000$ m/s. The dotted line depicts the expected dispersion for a pure azimuthal mode and a 15° tilt angle with respect to the azimuthal plane, consistent with the observation of "ionization spokes" seen in earlier Hall discharge devices. A second mode is that associated with axial disturbances at higher frequencies, the strongest of which are identified on the figure by superimposing dashed-dot vertical lines. The third mode that is identifiable in Fig. 5. is that of an $m = 12$ azimuthal wave (guided by the theoretical dashed line), which has a wavelength equal to that of the separation between the two probes, and is believed to be activated by the placement of the probes within the discharge annulus (30° separation results in a wavelength of $1/12^{\text{th}}$ the channel circumference). Finally, the fourth mode identified by the solid ($m=4$) line appears actually as a lower velocity limit to the high frequency disturbances. The appearance of this demarcation is attributed to an interaction between the axial disturbances and the four-fold azimuthal asymmetry imposed by the four equally spaced magnetic solenoids connected to the outer pole-piece. It is noteworthy that the dispersion characteristics of the disturbances are seen to vary dramatically with changes in operating regimes (e.g., applied voltage), or changes in position within

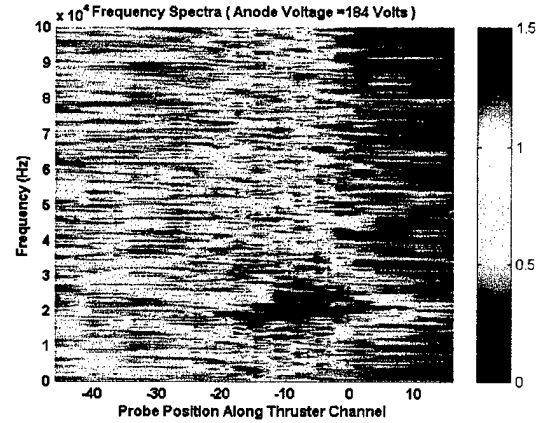


Fig. 4. Spectral map of plasma density fluctuations in the channel of a Hall thruster. The maximum color scale represents fluctuations in density that are comparable to the mean value.

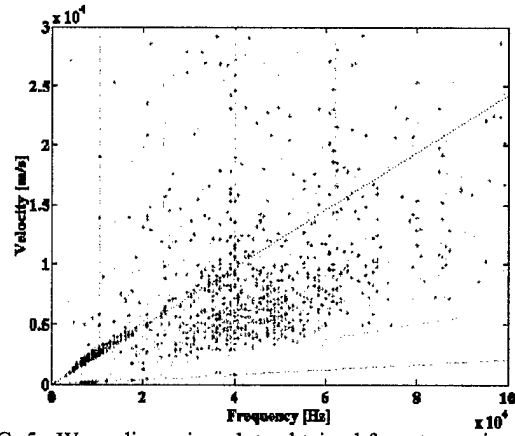


FIG. 5. Wave dispersion plots obtained from two azimuthal probes separated by 30° , for low discharge voltage conditions (100 V), and at $x = 0$ mm. The lines shown are the expected theoretical dispersion lines for azimuthal waves with mode numbers: an apparent $m = 0$ mode (vertical dot-dashed lines), $m = 1$ (dotted line), $m = 4$ (solid line), and $m = 12$ (dashed line) modes.

the discharge channel. The support under the ASSERT program has led to these initial studies of plasma instabilities in Hall thrusters. Because of these initial studies, we have attracted foreign visitors who are now continuing with the initial studies performed by Schmidt (E. Chesta, N. Gascon), who are funded in part by external fellowships.

Diagnostics of a Hybrid Arcjet-Hall Cluster

We believe that a propulsion device with a moderate thrust and moderate specific impulse will be able to fulfill a niche between the performance of arcjets and Hall thrusters. A propulsion system with those parameters can be constructed by using an arcjet as the neutralizer for a Hall thruster. Since the arcjet is a high ionization device that can generate large electron currents, it can provide the currents needed to neutralize a cluster of moderate power Hall thrusters. A schematic and photograph of this concept is shown in Fig. 6 and 7. Figure 8 shows the predicted performance of a cluster of 4 SPT-140s neutralized by one arcjet, operating on helium as a propellant. An efficient arcjet allows for higher thrust, higher specific impulse, and overall higher cluster efficiency. For these reasons, the helium arcjet was chosen as the neutralizer due to its high thrust efficiency [4,5]. Compared to a cluster of Hall thrusters at the same thrust level, the hybrid arcjet-SPT cluster has a lower mass and lower power at the expense of a moderate specific impulse and slightly lower overall efficiency.

There are a number of challenges to overcome in developing and demonstrating the hybrid arcjet-SPT thruster. First, there are very few vacuum systems that can handle both thrusters running simultaneously. The system needs to be able to pump tens of milligrams per second of helium while maintaining the low background pressures of 10^{-4} Torr needed for Hall thruster operation. Secondly, helium arcjets have a narrow stability range. The arcjet used in these studies was originally designed for other propellants, and the arc voltage randomly fluctuates when it is operated with helium. Finally, the predicted performance envelope shown in the figures is predicated on the assumption that the performance of a He arcjet is not compromised when its plume is providing the necessary current to neutralize the Hall thruster cluster. The development of diagnostics for studying the performance and structure of a He arcjet plume (see Appendix III) was motivated in part by the need to understand how this structure is altered when it is supplying the many tens of amps of electron current to neutralize the Hall discharges. An extensive LIF study of He arcjet plumes has been accomplished and has been submitted for publication, as shown in Appendix III. In continuing studies, our goal is to demonstrate the feasibility of drawing the needed current from a He arcjet plume, and to characterize (using LIF) the effects that it has on arcjet performance. So far, at the time of preparing this report, we have studied the changes in the arcjet operation and performance as current is drawn to a "surrogate" anode, since we do not have a facility operating at this moment to provide the pumping speed and pressure for both a working Hall discharge and an arcjet simultaneously. As shown below, preliminary findings are quite encouraging, as we have found that the arc voltage changes (slightly) as current is drawn to the surrogate anode, but the arcjet performance, as characterized by impact pressure probes and preliminary LIF is not compromised.

Fig. 6 and 7 shows the schematic and photograph of the setup used to characterize the effects of neutralization. The Hall thruster is represented by a 15 cm copper substrate. The substrate, which is referred to as a surrogate anode, is connected to a DC power supply. The current drawn by the power supply is measured across a shunt resistor. The performance of the arcjet is measured with an impact pressure probe, sitting on a translation stage, placed near the exit plane. This probe is water cooled so that it can withstand the plume environment. The pressure is measured after pausing up to 20 seconds and then taking an average of 1000 samples from a capacitance manometer. The thrust is

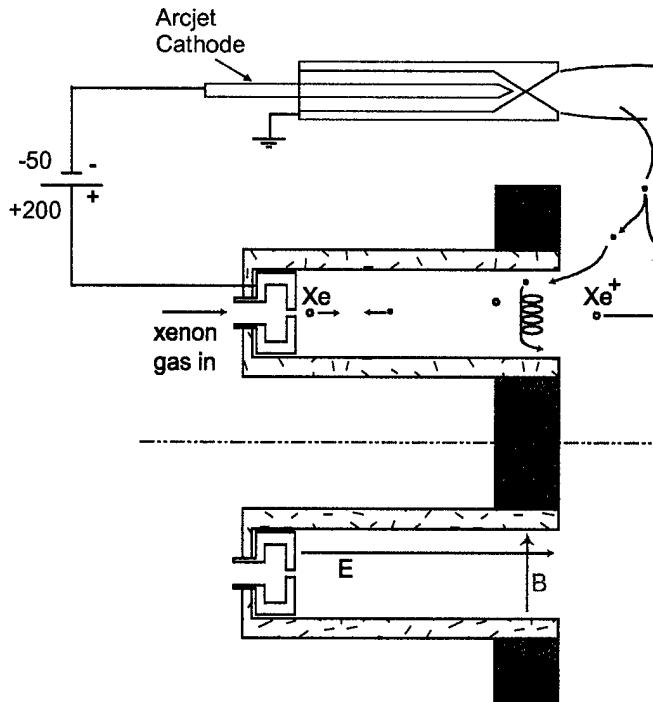


Figure 6. The hybrid arcjet-SPT concept

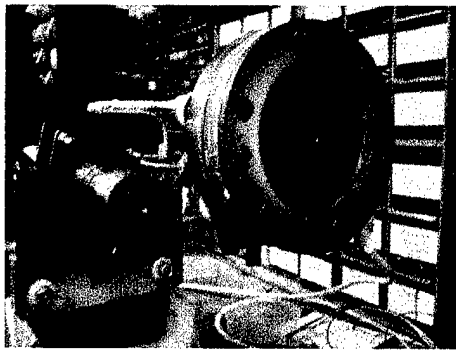


Figure 7. Arcjet with the copper substrate that serves as the surrogate anode

obtained by integrating the pressure profile across the nozzle. This measured thrust is found to agree well with the thrust measured from a thrust stand [5].

The results of these experiments demonstrate that electron current can be extracted from the arcjet without a severe degradation in the arcjet performance, but with a change in the arcjet operating conditions. First, the surrogate anode was used to extract currents from the arcjet to demonstrate changes in the arcjet operating conditions. Figure 9 shows the current drawn to the surrogate anode as the voltage of the surrogate anode is increased. At both arcjet propellant flow rates, the extracted current is greater than the arc current of 10.3 A. Up to 20% more current can be extracted in both cases. Also, there appears to be a threshold voltage for extracting large currents. Above this threshold, the anode current jumps from near 2 A to near 10 A. It is difficult to extract currents between those limits at steady state. With an increase in the mass flow rate, this threshold voltage decreases. At higher anode voltages, arcing occurs between the arcjet, surrogate anode, and the vacuum chamber.

The arcjet operating conditions change as current is extracted from it. Figure 10 shows the percent change in voltage as the voltage applied to the surrogate anode is increased. There are two different trends evident for the different mass flow rates. In each case, the arc

voltage decreases up to 20%. At the lower mass flow rate, the arc voltage recovers as the surrogate

Table 2. Thrust measurements

Flow Rate (mg/s)	Arc Voltage (V)	Arc Current (A)	Arc Thrust (mN)	Bias Voltage (V)	Bias Current (A)	Specific Impulse (s)
36.1	67	10	163	0	0	461
36.1	55	10	157	50	13	444
27	55	10	122	0	0	459
27	49	10	124	50	13	471

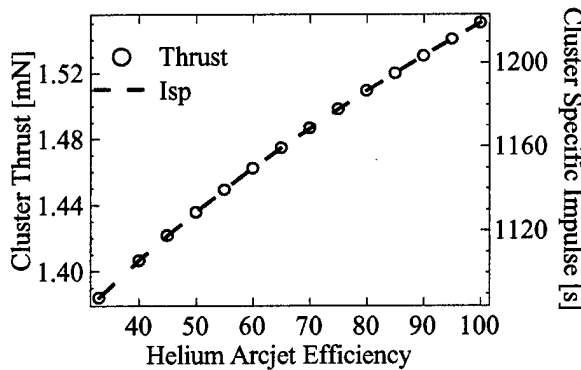


Figure 8. Cluster Thrust and Specific Impulse vs. Helium Arcjet Efficiency

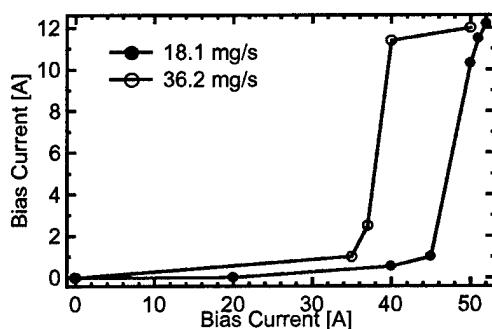


Figure 9. The current drawn to the surrogate anode as its voltage changes with the arcjet operating at the given mass flow rate and an arc current of 10.3 A

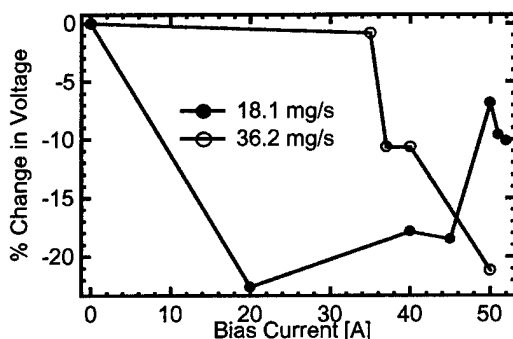


Figure 10. The change in arc voltage as the surrogate anode voltage changes

anode voltage increases. Previous experiments with hydrogen and nitrogen propellants show trends that agree with the higher mass flow rate—the arc voltage decreases with increasing surrogate anode voltage. The reason for the different trend for the lower mass flow rate is not yet clear. Nevertheless, these figures demonstrate that the arcjet can provide electron currents with an appreciable change in its operating condition.

As previously mentioned, the thrust was measured using an impact pressure probe. Table 2 shows the measured thrust for two flow rates with and without an applied surrogate anode voltage. The bias voltage and current listed in the table refer to the voltage and current of the surrogate anode. With an applied voltage, the current extracted was 30% greater than the arc current in both cases. The measured thrust slightly decreased at the higher mass flow rate, but slightly increased at the lower mass flow rate. Nevertheless, the thrust measured with the bias voltage is within the error of the measurement without a bias. During these measurements the extracted current decreased when the impact pressure probe was near the centerline of the flow. Although this will impact the measurements, the center of the arcjet flow field contributes little to the calculated thrust.

This project has demonstrated that current can be extracted from the arcjet without appreciable changes in the performance of the arcjet. 130% of the arc current can be extracted. Although the arc voltage changes by up to 20 %, the thrust remains constant.

The next phase will be an attempt for a small-scale demonstration. Our vacuum facilities can pump up to 2700 sccm of helium with 20 sccm of xenon while maintaining a background pressure of 10^{-3} Torr. A low-power (<100 W) arcjet from previous work will be used to neutralize one of our laboratory Hall thrusters. These are the first steps in the demonstration of the hybrid arcjet-SPT thruster that will fulfill the role of a moderate thrust and moderate specific impulse propulsion system.

References

1. "A Low-Power, Linear-Geometry Hall Plasma Source with an Open Electron-Drift," D.P. Schmidt, N.B. Meezan, W.A. Hargus, Jr., and M.A. Cappelli, *Plasma Sources Sci. Technol.* **9**, 68-76, 2000.
2. "Laser-induced fluorescence study of a xenon Hall thruster," R.J. Cedolin, W.A. Hargus, Jr., P.V. Storm, R.K. Hanson, and M.A. Cappelli, *Applied Physics B: Laser and Optics*, **65**, pp. 459-469, 1997.
3. "Characterization of Plasma Disturbances in a Hall Discharge using a Double Probe," D. P. Schmidt, N.B. Meezan, and M. A. Cappelli, AIAA-99-3437, 30th Plasmadynamics and Lasers Conference, AIAA 99-3603, Norfolk, VA, June 28-July 1, 1999.
4. Welle, R., Pollard, J., Janson, S., Crofton, M., and Cohen, R., "One Kilowatt Hydrogen and Helium Arcjet Performance," The Aerospace Corporation, 1993.
5. Walker, Q., Hargus, Jr., W., and Cappelli, M., "Characterization of a Low-Power Helium Arcjet," AIAA-98-3636, 34th Joint Propulsion Conference, 1998.

Acknowledgements

The P.I. would like to express his gratitude to the Air Force for augmentation support through this ASSERT grant. The research funded under this grant has contributed directly to the stipends of D. Schmidt and Q. Walker. The views and conclusions contained herein are those of the authors and should not be interpreted as necessarily representing the official policies or endorsements, either expressed or implied, of the Air Force Office of Scientific Research or the U.S. Government.

Publications Supported from this Grant

Archival Publications

1. "A Low-Power, Linear-Geometry Hall Plasma Source with an Open Electron-Drift," D.P. Schmidt, N.B. Meezan, W.A. Hargus, Jr., and M.A. Cappelli, *Plasma Sources Sci. Technol.* **9**, 68-76, 2000.
2. "Laser-Induced Fluorescence Characterization of a Helium Arcjet Flow," Q.E. Walker and M.A. Cappelli, submitted to *Applied Optics*, June 2000.
3. "A Characterization of Plasma Fluctuations within a Hall Discharge," E. Chesta, C. Lam, N.B. Meezan, D.P. Schmidt, and M.A. Cappelli, accepted to *IEEE Transactions on Plasma Science*, 2001.

Conference Papers/Presentations

4. "Electron Transport in Hall Thrusters," N.B. Meezan, D.P. Schmidt, W.A. Hargus, Jr., and M.A. Cappelli, NASA/JPL Advanced Rocket Propulsion Research Workshop, Huntsville, AL, April, 1999.
5. "Affecting Electron Transport in a Laboratory Hall Thruster," N.B. Meezan, D. Schmidt, M. A. Cappelli, and W. A. Hargus Jr., AIAA-99-2284, 35th Joint Propulsion Conference, Los Angeles, CA, June 20-24, 1999.
6. "Continued Development of a Linear Hall Thruster," M.A. Cappelli, D. Schmidt, N. B. Meezan, and W.A. Hargus Jr., AIAA-99-2569, 35th Joint Propulsion Conference, Los Angeles, CA, June 20-24, 1999.

7. "Characterization of Plasma Disturbances in a Hall Discharge using a Double Probe," D. P. Schmidt, N.B. Meezan, and M. A. Cappelli, AIAA-99-3437, 30th Plasmadynamics and Lasers Conference, AIAA 99-3603, Norfolk, VA, June 28-July 1, 1999.
8. "Laser Induced Fluorescence Measurements of a Helium Arcjet Flow," Q.E. Walker and M.A. Cappelli, AIAA 99-3603, 30th Plasmadynamics and Lasers Conference, Norfolk, VA, June 28-July 1, 1999.
9. "LIF Measurements of a Low-power Helium Arcjet," Q.E. Walker and M.A. Cappelli, 26th IEEE International Conference on Plasma Science, Monterey, CA, June 20-24, 1999.
10. "Anomalous Transport in Closed and Open-Drift Hall Discharges," Mark Cappelli, Nathan Meezan, and Dan Schmidt, 52nd Annual Gaseous Electronics Conference, American Physical Society, Norfolk, VA, October 5-8, 1999. See also Bull. Am. Phys. Soc. **44**, 59, 1999.
11. "Laser Induced Fluorescence Measurements of a Helium Arcjet Flow," Q.E. Walker and M. A. Cappelli, 41st Annual Meeting of the Division of Plasma Physics, American Physical Society, New Orleans, LA, November 16-20, 1999. See also Bull. Am. Phys. Soc. **44**, 29, 1999.
12. "Dispersion of Low Frequency Azimuthal Waves in Hall Discharges," M. A. Cappelli, D.P. Schmidt, and N.B. Meezan, 41st Annual Meeting of the Division of Plasma Physics, American Physical Society, New Orleans, LA, November 16-20, 1999. See also Bull. Am. Phys. Soc. **44**, 61, 1999.
13. "Impact Pressure Measurements of a Helium Arcjet Flow," Q.E. Walker and M. A. Cappelli, 42nd Annual Meeting of the Division of Plasma Physics, American Physical Society, Quebec City, Quebec, October 23-27, 2000. See also Bull. Am. Phys. Soc. **45**, 92, 2000.

Appendix I

A Low-Power, Linear-Geometry Hall Plasma Source with an Open Electron-Drift

D.P. Schmidt, N.B. Meezan, W.A. Hargus, Jr., and M.A. Cappelli

Plasma Sources Sci. Technol. **9**, 68-76, 2000

A low-power, linear-geometry Hall plasma source with an open electron-drift

D P Schmidt, N B Meezan, W A Hargus Jr and M A Cappelli†

Mechanical Engineering Department, Thermosciences Division, Stanford University, Stanford, CA 94305-3032, USA

Received 30 July 1999, in final form 6 December 1999

Abstract. This paper presents a discussion of the physics of modern Hall plasma thrusters and its impact on the design of new plasma thrusters of varying geometry and power. A particular emphasis is placed on the design and development of a linear-geometry (non-coaxial) source with an open electron-drift current. The operating characteristics of a linear-geometry Hall discharge scaled to operate in the 50 to 100 W power range are presented. Two thruster acceleration channels were fabricated—one of alumina and one of boron nitride. Differences in operation with the two channel materials are attributable to differences in the secondary electron emission properties. In either case, however, operation is achieved despite the lack of a closed electron current drift in the Hall direction, suggesting that there is an anomalous axial electron mobility, due to either plasma fluctuations or collisions with the channel wall. Strong low-frequency oscillations in the discharge current, associated with the depletion of propellant within the discharge, are seen to appear and vary with changes in the applied magnetic field strength. The frequency of this oscillatory mode is higher than that seen in larger (and higher power) discharges, due to the decreased residence time of the propellant within the channel.

1. Introduction

Hall discharge plasma accelerators have been considered for use in satellite propulsion since the early 1960s [1, 2]. In a Hall plasma source, a low-pressure discharge is sustained within a bounded dielectric channel in crossed electric and magnetic fields. Electrons emitted from a cathode external to the channel, or created by the ionization processes, drift along the channel towards the anode located at the channel base. The anode also serves as the source of neutral propellant (typically xenon). The radial component to the magnetic field is designed to be a maximum near the channel exit, and in this region, the electrons become highly magnetized, as the classical electron Hall parameter is much greater than unity. In typical Hall discharge plasma sources, the geometry is co-axial (figure 1) with an annular channel and surrounding solenoids generate a radial magnetic field. In this co-axial configuration, the electrons are constrained to move in the azimuthal direction of the closed $E \times B$ drift, with cross-field drift providing the necessary electron current to sustain the discharge. As the electron Hall parameter is much greater than unity, the Hall current density can be many orders of magnitude greater than the axial current density. According to classical electron transport theory, electrons can circle the annular channel in the Hall direction many times before being captured at the anode. A co-axial geometry therefore allows for this 'closed' electron

drift in the Hall direction, and uninterrupted Hall current. The region of trapped electrons acts as a volumetric zone of ionization that in some devices may occupy a small fraction of the overall channel length. The ions generated in this region, unaffected by the magnetic field because of their large inertia, are accelerated by the electric field resulting from the impeded electron flow, producing thrust. Very high ionization fractions and ion velocities can be generated with these discharges and, due to their high efficiencies and high specific impulse, Hall plasma thrusters in the 1–5 kW power range are being evaluated for use on commercial, military and research spacecraft [3].

A precise theory is lacking for the mechanism of cross-field electron transport in Hall plasma thrusters. Early experiments on Hall plasma sources indicated that classical electron transport theory could not account for the measured 'anomalous' axial (cross-field) electron current densities. Janes and Lowder [2] drew attention to the presence of density and electric field fluctuations within the channel of a Hall discharge, and first suggested that these plasma disturbances enhance the axial electron current. Indirect measurements of the 'effective' Hall parameter as a result of these fluctuations were in agreement with the anomalous transport coefficient first identified by Bohm *et al* [4], which characterizes the process now widely recognized as 'anomalous' Bohm diffusion [5]. The Bohm mechanism predicts an electron mobility that scales inversely with the magnetic field strength (as opposed to the classical B^{-2} scaling), and an effective

† Author to whom correspondence should be sent.

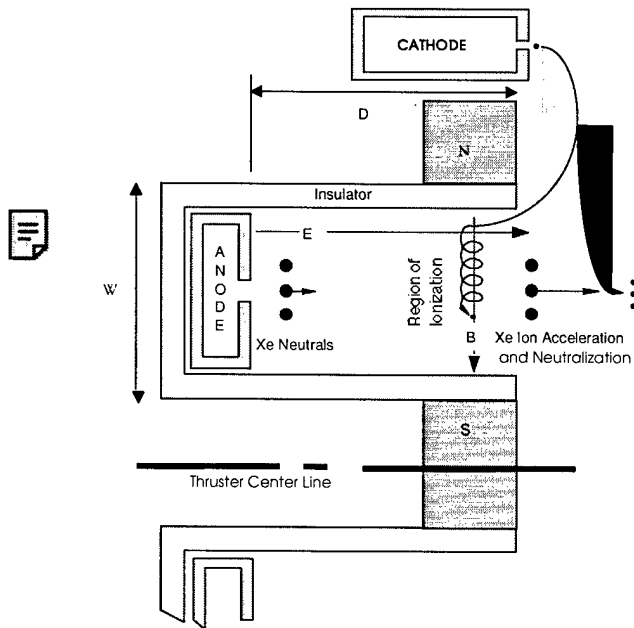


Figure 1. Schematic illustration of a typical co-axial Hall discharge.

electron Hall parameter of about 16. At conditions typical of Hall plasma thrusters near the region where the magnetic field is strongest, the classical Hall parameter is about 500–1000. A value of 16 represents a significant enhancement in the cross-field drift, and indicates that the ratio of Hall current density to axial current density may be much less than that suggested by classical transport theory. While an enhanced electron current due to fluctuations is one possible mechanism for enhanced electron transport, the operation of modern Hall plasma thrusters seems to depend significantly on the properties of the dielectric wall [6]. Previous researchers have proposed the possibility of an enhanced ‘near-wall conductivity’ due to the ‘wall scattering’ of electrons. While it seems the precise knowledge of which mechanism is responsible for transport is necessary to properly scale a Hall discharge, we show below that either of these mechanisms exhibits the necessary dependence on discharge parameters to achieve a desired scaling in discharge size or power.

Despite the progress that has been made in the development of co-axial Hall plasma thrusters that operate in the kilowatt power range, a need has developed for low-thrust, high-efficiency propulsion devices to be used for precise orbit control on small, power-limited satellites. A low-power (10–100 W) Hall thruster could fill this need. The proper scaling of a Hall plasma thruster for efficient operation at such low powers requires a renewed examination of the discharge physics that controls thruster performance. Also, alternative geometries that can potentially reduce thruster mass and/or size should be investigated. The scaling of co-axial Hall thrusters to lower powers has been discussed previously in the literature [7, 8]. To our knowledge, however, no one has reported on the operation of a Hall plasma source with a linear geometry and hence an open electron-drift. The

merits of a linear-geometry thruster are appealing, although any discharge model based on either classical or ‘Bohm’ electron transport indicates that even for moderate aspect ratios (depth to channel length ratio, D/L), such a geometry would interrupt the electron Hall current. A linear geometry allows compact packaging of the thruster in a limited space, making the magnetic circuit amenable to the use of permanent magnets. Also, a multiple array of linear thrusters could be efficiently stacked in order to extend the operating envelope of the propulsion system. This modular approach could be used to maintain operation at maximum efficiencies by simply turning stacked low-power linear thrusters on and off as needed to change the thrust level rather than by changing the operating point of a single thruster.

In this paper, we discuss the design and operation of a low-power linear-geometry Hall plasma thruster based on scaling arguments that we have presented previously [8]. The linear thruster tested here is scaled to operate at a power level that is 10–15% that of co-axial discharges built and tested in our laboratory in previous years [9, 10]. The linear-geometry, non-coaxial Hall plasma thruster has been fabricated and operated at near-design conditions. Operating characteristics are presented for both alumina and boron nitride acceleration channels for a range of peak magnetic field strengths.

2. Review of Hall thruster physics

Modern co-axial Hall plasma thrusters that operate in the 1–5 kW power range have been shown to operate with very high thrust efficiencies—around 50%. These thrusters have acceleration channel diameters ranging from 50 to 280 mm. One feature common to these thrusters is that the channel width (W) is approximately 15% of the outer diameter, which itself is about twice the acceleration channel depth (D). In scaling these discharges to operate at various power ranges, it is often desirable to preserve the geometrical relationship between channel width, diameter, and depth, although the physical basis for the commonly used geometrical parameters is not well understood.

In a typical Hall thruster, the magnetic field near the channel exit is sufficient to trap the electrons in cyclotron motion. The electron orbit radius (Larmor radius) is generally smaller than the electron mean free path λ and the acceleration channel width W . In this way, the electrons are confined to the magnetized portion of the plasma discharge. The Larmor radius, being dependent on particle mass, is much larger for ions, so they are largely unaffected by the magnetic field. The electron Larmor radius, r_e , scales as:

$$r_e \sim \frac{T_e^{1/2}}{B} \quad (1)$$

Here B is the magnetic field strength and T_e is the electron temperature. In the design of a low-power (and hence presumably smaller) discharge, a decrease in W requires a corresponding decrease in r_e . The magnetic field strength can be tailored for proper scaling; however, the electron temperature is not easily adjusted, as it is a consequence of a more complex relationship between geometry and operating conditions. The electron temperature is established

through a balance between ohmic dissipation, electron-particle collisions (including ionization), and electron-wall collisions. It was decided instead to scale the magnetic field strength as necessary and apply reasonable scaling arguments to preserve the mean electron energy from one design to another. It is seen from (1) that if the electron temperature is to be preserved in the scaling to lower powers, reducing the characteristic size of the thruster requires a concomitant increase in the operating magnetic field strength.

In a Hall discharge's use as a propulsion device, it is desirable to efficiently utilize the propellant, by achieving as high an ionization fraction possible. In scaling a higher power Hall discharge to lower powers, it is therefore desirable to preserve the ratio of the characteristic time to ionize the propellant to the residence time of the propellant in the discharge channel. The ionization time can be found from the inverse of the volumetric rate of ionization R_i , which scales linearly as the electron and neutral densities (n_e and n_a):

$$R_i = n_e n_a \alpha_i(T_e). \quad (2)$$

Here, $\alpha_i(T_e)$ is the temperature-dependent electron impact ionization rate coefficient. The characteristic time for ionization is $\tau_i = n_e/R_i$:

$$\tau_i = 1/n_e \alpha_i. \quad (3)$$

The residence time for a neutral atom can be found by dividing the acceleration channel depth D by the velocity of the neutrals, so it is expected to scale as:

$$\tau_R \sim D/T_a^{1/2}. \quad (4)$$

Here, T_a is the neutral xenon temperature, which is assumed to be relatively uniform, and which will largely control the gas dynamic behaviour of the neutrals within the channel. The ratio of these two parameters, the ionization time over the residence time, scales as

$$\frac{\tau_R}{\tau_i} \sim D n_a \quad (5)$$

where we assumed that the neutral xenon temperature (along with the electron temperature) is invariant to scale. As we shall see, this assumption regarding the invariance in T_a may be tenuous, since the xenon temperature will depend on the anode and channel wall temperatures, both of which are likely to be considerably higher for a low-power device because of the geometric scaling conclusions arrived at below. A consequence of (5) is that a geometric reduction in the channel depth requires a corresponding increase in the neutral density to preserve the ratio of time scales. As we shall see from the next section, this density increase is achieved by properly scaling the mass flow rate and the channel area.

The axial variation in the magnetic field is also known to have a large impact on discharge performance. In a modern co-axial Hall thruster, the radial magnetic field is sharply peaked near the exit of the acceleration channel, with a distribution width that is much less than the channel depth. A high magnetic field near the anode can lead to a large anode fall loss as electrons experience resistance to current flow. Since magnetic fields are difficult to shape, especially for co-axial designs, the depth of the channel is often dictated more

by the magnetic field distribution than geometric scaling of the channel length. An advantage of a linear geometry over a co-axial one is the ease at which a desired magnetic field distribution can be achieved with a less complicated magnetic circuit.

3. Thruster scaling implications

Based on the physics presented in the previous section, the scaling of the discharge is relatively straightforward. We treat the desired discharge voltage ϕ_d as a design parameter, as it directly determines the ion velocity (and hence specific impulse of the thruster), which is often dictated by the satellite mission objectives.

We continue with the assumption that the electron temperature can be preserved with proper scaling. This is justified if we can argue that for a reduction of the total power by some factor ζ , the rates of energy loss and thrust power are correspondingly reduced by the same factor. The reduction in discharge power without a reduction in the discharge voltage implies a reduction in the overall discharge current. However, for proper geometric scaling, the area is correspondingly reduced by the factor ζ^2 , so the current densities must be increased by the factor $1/\zeta$. The necessary scaling in the ion current density (and hence thrust power) is achieved if the plasma density is correspondingly increased, since the velocity is unchanged. The necessary scaling in the axial electron current density is achieved if the axial electron drift velocity, V_{ed} , is arguably scale-invariant. As we have discussed previously [8], both the anomalous Bohm transport and wall collisions will give rise to drift velocities that are scale-invariant. The axial drift velocity associated with Bohm transport is determined by the ratio of the electric field strength, E , to the magnetic field strength

$$V_{ed \text{ Bohm}} = \frac{e}{16B} E \sim \frac{E}{B} \quad (6)$$

which will be preserved through a geometric scaling. If the cross-field transport is largely controlled by wall collisions, then, for highly magnetized electrons ($\omega_{ce} = eB/m_e \gg \nu_{wall} = C_e/W$, the wall scattering frequency), the axial electron drift velocity is approximately

$$V_{ed \text{ Wall}} = \frac{eE\nu_{wall}}{m_e\omega_{ce}^2} \sim EW \quad (7)$$

which will also be preserved with the proper geometric scaling since the magnetic field scales as $B \propto 1/W$, as discussed earlier (here, C_e is the mean thermal electron speed, which is preserved if the temperature is preserved, and e and m_e are the charge and mass of the electron, respectively). The increased electron number density (by the factor $1/\zeta$) is achieved because the corresponding decrease in the mass flow rate results in an increase in n_a , since the area is decreased by the factor ζ^2 . This relies on the assumption that the ionization fraction is preserved, which is reasonable if the ratio of time scales presented in (5) is also preserved.

Finally, in order to preserve the electron temperature, we must argue that the electron energy loss rates will also scale in proportion to the decrease in power. It is easily shown that

the necessary scaling is obtained if the dominant energy loss mechanism is through wall collisions. It is noteworthy that volumetric ionization will also satisfy the scaling condition, since the energy loss rate through ionization is

$$E_i = n_e n_a \alpha_i V_c \varepsilon \sim \zeta. \quad (8)$$

Here, V_c is the channel volume and ε_i , the ionization energy of xenon.

One undesirable consequence of the geometric scaling for operation at reduced power levels is an increase in heat flux to the channel walls [7]. Since the power is reduced by the scaling factor ζ and the wall area reduced by ζ^2 , the heat flux to the walls will increase by a factor of $1/\zeta$. This scaling consequence may prove problematic for very low-power (and consequently reduced size) Hall plasma thrusters.

It is noteworthy that the decreased residence time of the neutral xenon in the channel (see (4)) should result in a shift to high frequencies in the characteristic breathing instability often seen in the 7–10 kHz frequency range in higher power devices [11]. While we predicted this shift in an earlier paper [8], the poor performance of the low-power thruster presented in that study precluded such a measurement. We have characterized the current oscillations in the discharge reported on here, and have found the oscillation frequencies to be consistent with the nearly $1/10$ scaling carried out in this study.

In summary, if it is desired to scale the power of a Hall thruster by some arbitrary factor ζ , then the characteristic scale lengths of the thruster and mass flow rates should be scaled by the same factor, ζ . The appropriate adjustment to the magnetic field (preserving its shape) is to increase it by the factor $1/\zeta$. With these scaling laws, according to the arguments presented above, the electron temperature should be preserved, as well as the ratio of electron current to ion current.

4. Linear geometry implications

In a weakly collisional steady-state plasma, where the electron Hall parameter satisfies the condition

$$\omega_{ce} \tau_e \gg 1 \quad (9)$$

the ratio of the cross-field (axial) electron current to the Hall current is

$$\frac{J_{ez}}{J_{eH}} = \frac{1}{\omega_{ce} \tau_e}. \quad (10)$$

Here, τ_e is the time between electron collisions. If we use the classical electron collision time in (9), we would find that for most modern thrusters, the resulting Hall parameter is typically in the range of 100–1000. Note that the current ratio described in (10) is a scale invariant in that the scaling laws introduced here would increase the electron cyclotron frequency in proportion to the decrease in the electron collision time. It is precisely this vast inequality between the axial and Hall currents which prompted the use of a co-axial design in early thrusters since, as mentioned above, a co-axial geometry with a closed electron drift allows the electrons to traverse the annulus many times prior to anode capture.

The presence of an anomalous electron transport mechanism, whether fluctuation or possibly wall-scattering induced, reduces the demand placed on the ratio of the Hall to axial electron current. A value of 16 for the 'effective' Hall parameter, as suggested by the anomalous Bohm mobility, still implies an electron drift direction that is predominantly in the direction of the crossed electric and magnetic field. However, we note that the value of 16 for the Bohm coefficient is strictly speculative, as the effective Hall parameters in modern Hall thrusters have not been accurately characterized, and coefficients within a factor of two or three of this value have been obtained for other plasma devices [5]. It is therefore conceivable that the Bohm coefficient can be less than this value. If so, then the necessity for a closed electron drift is removed, and with an adequate aspect ratio (ratio of channel length to channel depth), a linear Hall thruster with an open electron drift may perform equally well in comparison to closed-drift designs. However, even with an effective Hall parameter of unity, the linear design does impose an asymmetry in the electron flow, giving rise to expected asymmetric current densities within the channel that may impact on discharge performance.

5. Experiment

5.1. Test facility

The Stanford high vacuum test facility has been discussed extensively elsewhere [8–10]. It consists of a non-magnetic stainless steel tank approximately 1 m in diameter and 1.5 m in length. The facility is pumped by two 50 cm diffusion pumps, backed by a 425 l s^{-1} mechanical pump. The base pressure of the facility is approximately 10^{-6} Torr as measured by an ionization gauge uncorrected for mass species. Thruster testing at xenon flow rates of 2–5 sccm results in chamber background pressures in the region of 4×10^{-5} Torr. This indicates that the facility has a xenon gas pumping speed of around 2000 l s^{-1} . Propellant flow to the thruster anode and cathode is controlled by two Unit Instruments 1200 series mass flow controllers factory calibrated for xenon. The propellant used in this study was research grade (99.99%) xenon.

5.2. Linear Hall thruster

The design of the linear Hall thruster studied here is based on the scaling of a co-axial reference thruster recently built by our laboratory and operated at a nominal power of 400–700 W [12]. A scaling factor of $\zeta = 0.1$ was used in accordance with the scaling laws presented in the previous sections, although the performance of the magnetic circuit precluded the use of a channel depth that was one-tenth the depth of the reference coaxial discharge. The channel depth deviated from strict scaling laws in order to reduce the magnetic field strength at the anode, and hence the anode fall losses. A comparison of the coaxial thruster used for scaling and the linear thruster is shown in table 1. A schematic of the linear Hall thruster is shown in figure 2.

The magnetic circuit includes four 90 mm long electromagnet windings consisting of a 9.5 mm diameter core of commercially pure iron with 6 layers of 22 gauge

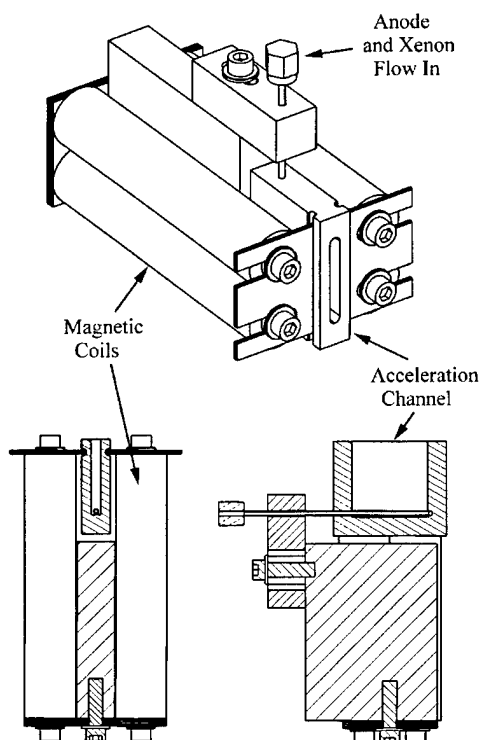


Figure 2. Schematic of the linear-geometry open electron-drift Hall discharge.

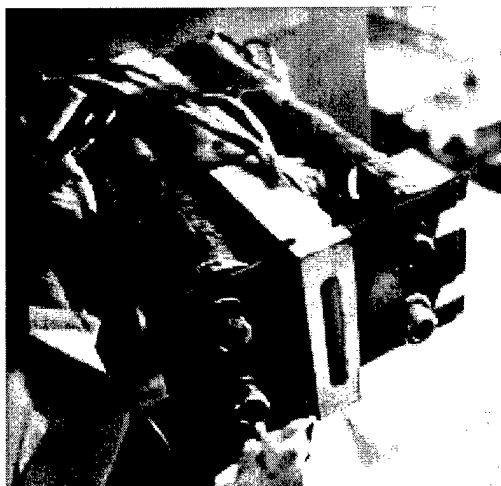


Figure 3. Photograph of the linear-geometry open electron-drift Hall discharge.

insulated copper magnet wire. The magnetic bottom plate is 3 mm thick silicon steel, whereas the magnetic top plate is 1.5 mm thick silicon steel. The discharge channel was fabricated in two versions, one constructed of high-purity alumina ceramic and the other of boron nitride. The anode is a 1.6 mm diameter stainless steel tube with 14 propellant holes, 0.2 mm in diameter spaced by 1.6 mm. A photograph of the thruster is shown in figure 3.

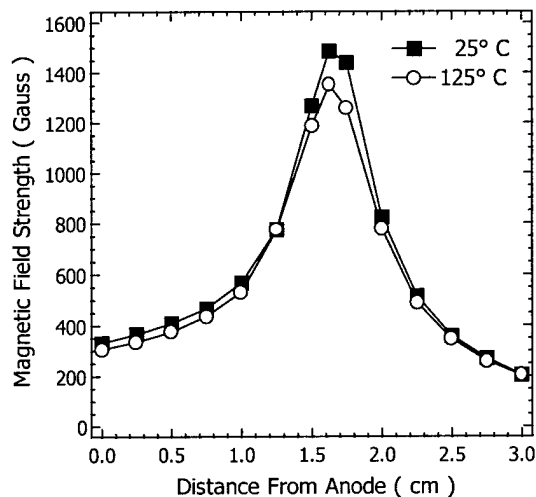


Figure 4. Transverse magnetic field strength variation with axial position. In both cases, the winding current is 1.25 A.

Measurements of the transverse component of the magnetic field show that the magnetic field near the anode is 23% of the peak value, which is located about 2 mm upstream of the channel exit. The measured field distribution for a winding current of 1.25 A is shown in figure 4 for two different temperatures. These measurements were obtained *ex situ*, by heating the entire thruster unit in an oven at ambient conditions while measuring the magnetic field strength. It can be seen that the peak value of 1500 G at room temperature drops to less than 1400 G with a 100 °C temperature rise. This is significant in that the temperature of the acceleration channel has been measured to be as high as 440 °C by embedded thermocouples during operation in the thruster fabricated out of boron nitride.

The cathode used to neutralize the ion beam and support the necessary electric field is an Ion Tech. Inc. HCN-252 hollow cathode. It is capable of supplying a maximum current of 5 A at xenon flow rates of 0.1 to 0.5 mg s⁻¹. It is mounted in front of the thruster such that the hollow cathode exit is 1 cm above the exit of the channel. The cathode is the exact same unit used in the higher power thrusters, and the flow rate used here is comparable to the flow rate through the thruster itself (2 sccm). We expect that the near exit plane xenon density due to the cathode flow will have a negative effect on the discharge performance. However, because the neutral gas density in this low power discharge is about a factor of 5–10 times that in the higher power prototype, the effect is expected to be no greater here than in the higher power version. No attempt at designing and fabricating an appropriately scaled cathode has been made, although the future development of low-power (< 50 W) Hall thrusters will rely on such a development.

The anode of the discharge is powered by a Sorensen SCR600-1.7 laboratory power supply capable of providing 600 V and 1.7 A. The anode also has a 4 Ω resistor in the power line to serve as ballast during initial start of the discharge. The cathode heating element is powered by a low voltage direct-current (DC) power supply capable of providing the 8.5 A required to heat the cathode for startup

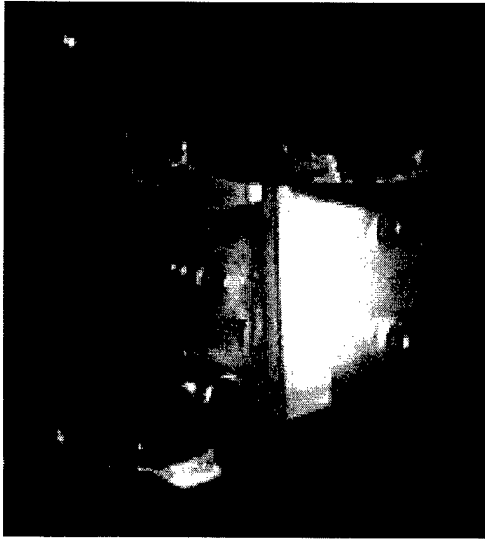


Figure 5. Photograph of the linear-geometry open electron-drift Hall discharge while operating.

and 4.0 A after start. The cathode flow rate of xenon was 2 sccm, a typical value used during operation of our higher power co-axial discharges. The cathode keeper uses a Sorensen SCR300-6 laboratory power supply to provide 250 V for initial cathode start and approximately 10 V and 250 mA during thruster operation. The power required for the magnetic circuit solenoids is provided by a Tektronix PS281 DC power supply operating in current limited mode.

The voltage and current of the thruster were recorded by acquiring data through a National Instruments PCI-5102 data acquisition card plugged into a desktop computer. A voltage divider was used so that the 5 V maximum voltage limit to the card was not exceeded while testing the thruster up to 250 V. The current was monitored by measuring the voltage drop across the 4 Ω ballast resistor.

6. Results and analysis

The thruster described was run at near-design conditions. To start the thruster, a glow discharge was initiated with the magnetic field turned off. With the power supply under current limit control and an upper limit set on the voltage, the magnetic field was increased. The discharge intensity greatly increased and changed colour from dull pink to a bright bluish emission as the magnetic field was increased, which is also typical of coaxial designs. A picture of the thruster running at design conditions is shown in figure 5. The voltage gradually increased until it reached the voltage limit setting. The power supply subsequently switched into voltage control, where most of the data reported was taken.

During operation at magnetic fields above 600 G, it was noted that the discharge was slightly asymmetric, being more intense near the side end of the channel in direction of the $E \times B$ electron drift. It was especially apparent during operation of the alumina thruster that this end wall became extremely hot and glowed intensely. This glow was contrasted to the bulk of the thruster channel, which did not show this intense

heating. On one occasion, after a few minutes of running the alumina thruster, the acceleration channel cracked along the edge of the glowing area. This failure was probably due to a high thermal stress caused by extreme temperature gradients in this region of the channel wall. Operation with the boron nitride thruster did not result in such a non-uniform temperature field on the insulating wall. This difference between the boron nitride and alumina insulators is attributed to the difference in the thermal conductivity values of the materials. The boron nitride channel end wall in the direction of the electron drift was instrumented with four embedded J-type thermocouples distributed along its length. During nominal operation at 1500 G and 0.7 A, the thermocouples registered temperatures in excess of 400 °C across the entire channel, with the side wall at around 440 °C.

Figure 6 shows the voltage (V)–current (I) characteristics recorded for both the boron nitride and alumina thruster channel for a range of magnetic field strengths and at a xenon flow rate of 2 sccm. The V – I characteristics for the boron nitride channel are somewhat typical of Hall discharges, with an ‘ionization branch’ at low currents and low magnetic field strengths, and a relatively steep ‘current saturation branch’ at high operating magnetic field strengths and high discharge current. However, these features are less distinct in the case of the alumina channel. In fact, the V – I characteristics do not show an obvious current saturation regime in this latter case. At relatively low magnetic field strengths, the V – I characteristics of the thruster with the alumina channel wall are nearly indistinguishable from that of the same thruster with a boron nitride wall. This is also the case for all magnetic field strengths investigated, at currents below about 0.5 A. Above these current levels, the V – I characteristics for the alumina channel thruster flatten out (note the apparent ‘knee’ in the figure), whereas the boron nitride channel thruster voltage rises sharply.

We speculate that secondary electron emission from the alumina channel is partly responsible for the interesting shape of the V – I characteristics. The possible influence of secondary electron emission in establishing the electron transport in Hall thrusters has been discussed in the prior literature [6, 11]. Alumina has a higher secondary electron emission coefficient than boron nitride [13] and, in addition, we expect that the secondary electron emission is sensitive to wall temperature. It was apparent that during thruster operation with the alumina walls, the wall temperature may have been sufficiently high to significantly enhance secondary electron emission. The higher secondary electron emission for the case of the alumina insulator wall would aid electron transport across the magnetic field. As a result, the thruster could not support as high a voltage as that supported by the thruster with the boron nitride wall. This conjecture would imply that there is a high electron flux (current) along the side wall opposite the direction of the electron Hall current, an argument that is consistent with the observation that the side wall of the boron nitride thruster is found to experience significant erosion. In a recent study by Raitses *et al* [6], it was noted that there were significant differences in the V – I characteristics of a thruster operating with a machinable glass channel and a boron nitride channel. In that study, enhanced axial transport in the thruster with

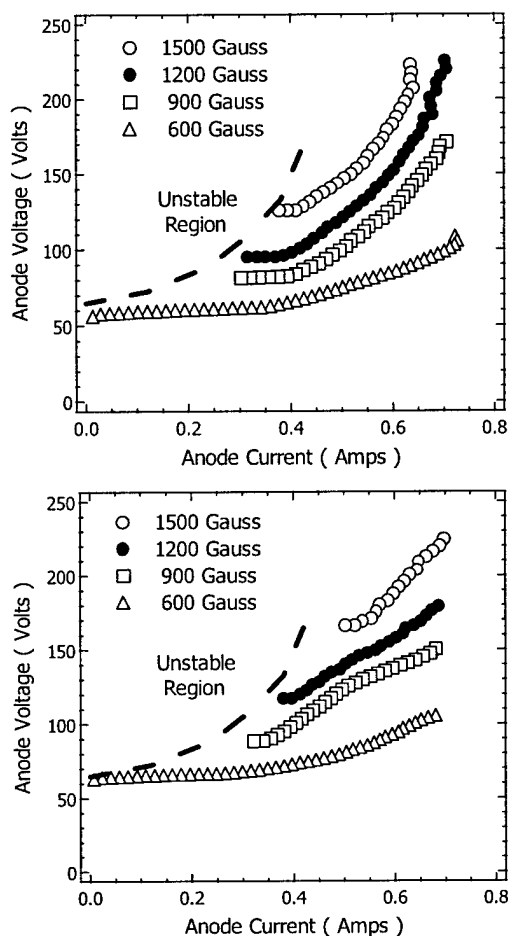


Figure 6. Discharge voltage-current characteristics of the linear-geometry Hall discharge (top) boron nitride channel, (bottom) alumina channel.

the machinable glass channel was attributed to wall effects, decreasing the thruster efficiency at high operating voltages. The qualitative findings reported on in this study agree with these past observations. It is also noteworthy that the conjecture that there is an enhanced electron current due to wall collisions is supported by the relatively poor efficiency of this discharge, as an upper limit of the ratio of the ion current to electron current is no more than 30%, based on full utilization (ionization) of the propellant.

In all cases, the thrusters exhibited a region of unstable operation. At all magnetic field strengths except the lowest value shown, the discharge had a low current limit in its operating envelope. Attempts to operate or start the discharge in this region would fail. We speculate that this region of instability is closely tied to the requirement for enhanced electron transport and that, at low currents and high magnetic fields, the anomalous transport process cannot provide the necessary current to maintain the discharge.

The fact that the thruster ran without a mechanism for closing the Hall current confirms the importance of an electron transport process that is due to plasma fluctuations and/or wall effects associated with secondary electron

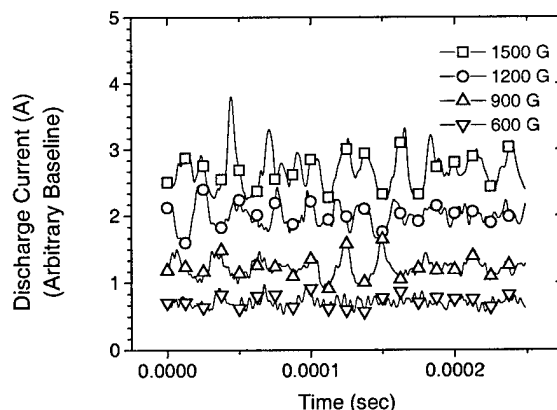


Figure 7. Time-variation in discharge current for the alumina-walled plasma source at a range of peak magnetic field conditions.

emission. As in the higher power co-axial discharges, the linear discharge studied here also exhibited plasma fluctuations, which were detected as fluctuations in the external circuit discharge current.

Figure 7 shows the oscillations in the discharge current of the linear thruster operating with the alumina channel wall for a range of peak magnetic field strengths and at a discharge current of 0.7 A. The fluctuations in the discharge current for the boron nitride wall were qualitatively similar. It is apparent that at low magnetic fields, there is a relatively low frequency oscillation, on which higher frequencies are superimposed. The low frequency oscillation increases in amplitude and in frequency as the magnetic field is increased. These intense low frequencies observed in this linear device are similar to those seen in co-axial devices, and are believed to be the so-called 'breathing' mode of oscillation associated with the neutral xenon transit through the ionization zone [14]. This instability is associated with the disturbance in the balance established between the depletion of neutrals in the channel as a result of ionization, and their replenishment. Since the length of the ionization zone in this low-power Hall discharge is scaled to be some 5-10 times shorter than that of our reference thruster, the frequencies of these disturbances are expected to be at least a factor of five higher than those seen in our higher power co-axial devices.

Figure 8 compares the Fourier analysis of the temporal fluctuations in discharge current of the reference 400 W (200 V, 20 sccm, 160 G, 2 A) co-axial thruster and the low-power linear thruster operating with the alumina channel wall (data shown in figure 7). It is apparent that the low-power thruster has a strong low-frequency mode, similar to that seen in the co-axial high-power devices, at frequencies that are approximately a factor of four times that of the higher power thruster. As the magnetic field is increased the frequency of the fluctuations in the anode current also increase, until a magnetic field strength of 900 G, beyond which it remains constant. This result is seemingly inconsistent with the theoretical predictions of Boeuf and Garrigues [14]. However, a direct comparison to the results in [14] is difficult to make, since in our studies, the current is held constant while the magnetic field is increased (resulting

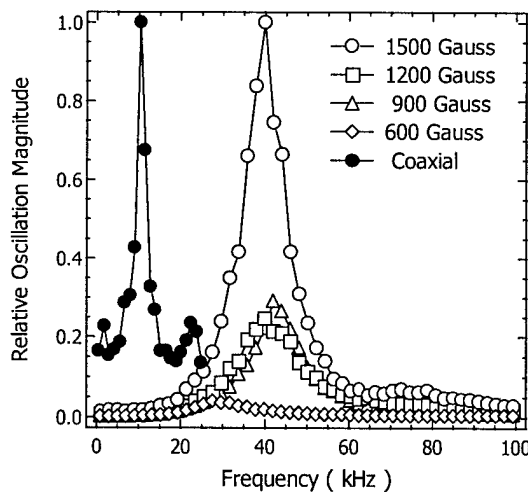


Figure 8. Low-frequency spectral analysis of the temporal fluctuations in the discharge current. Included in the figure is the spectral distribution of the fluctuations seen in the higher power co-axial discharge for comparison.

in increased discharge voltages). In the calculations of Boeuf and Garrigues, the voltage was varied at constant magnetic field (giving rise to varying current) and/or the magnetic field was varied at constant voltage. As discussed in [14], the frequency of this mode is seen to increase dramatically with voltage (at constant magnetic field). The response that we see is therefore likely to be a result of the response in the frequency to changes in both the voltage and the magnetic field.

It is interesting to note that at the highest magnetic field studied, there is a superimposed high-frequency oscillation at about 80 kHz. Through particle simulations, Boeuf and Garrigues [14] also discovered the presence of strong disturbances in the plasma density and electric field upstream near the anode when the magnetic field continues to persist near the anode. The weak intensities seen here at the highest magnetic field studied may be a consequence of these near-anode instabilities, although a precise characterization of these instabilities in a linear geometry must still be performed. In a related study, we have identified the presence of near-anode instabilities in this frequency range (40–100 kHz) in co-axial Hall discharges [15].

7. Summary

An analysis and arguments for the scaling of a Hall plasma thruster to low powers was presented. A linear-geometry version of a thruster operating in the 50–100 W power range has been fabricated and operated at near-design conditions. Preliminary results obtained so far indicate that at the scaled power levels, these low power plasma discharges operate at much higher channel wall temperatures. This increased heat flux may be a major impediment to the extended operation of very low power devices.

The linear Hall plasma thruster reported on here is found to have the characteristic discharge instabilities seen in higher power co-axial versions. Although we have not performed an

extensive analysis of the thruster performance, it does appear that the linear device behaves in many ways similarly to those of a co-axial design with a closed electron drift. Since the linear discharge operates without a closed Hall current, it suggests that there must be an anomalous mechanism for cross-field electron transport.

This device might prove most useful for investigating various materials for use as acceleration channels in Hall thrusters. The linear-geometry design allows easy fabrication from a variety of materials. A study of the operating characteristics of thrusters constructed with insulating walls fabricated from a wide variety of materials would be useful for understanding the effect of secondary electron emission on electron transport.

Acknowledgments

This work was supported by the Air Force Office of Scientific Research, with Dr Mitat Birkan as the contract monitor.

References

- [1] Brown C O and Pinsley E A 1965 *AIAA J.* **3** 853
- [2] Janes G S and Lowder R S 1966 *Phys. Fluids* **9** 1115
- [3] Gulczinski F S and Spores R A 1996 Analysis of Hall-effect thrusters and ion engines for orbit transfer missions *32nd Joint Propulsion Conference (1996, Lake Buena Vista, FL)* AIAA-96-2973
- [4] Bohm D 1949 *The Characteristics of Electrical Discharges in Magnetic Fields* ed A Guthrie and R K Wakerling (New York: McGraw Hill)
- [5] Chen F F 1985 *Plasma Physics and Controlled Fusion* 2nd edn (New York: Plenum) p 193
- [6] Raites Y, Ashkenazy J, Appelbaum G and Guelman M 1997 Experimental investigation of the effect of channel material on Hall thruster characteristics *25th International Electric Propulsion Conference (1997, Cleveland, OH)* IEPC 97-056
- [7] Khayms V and Martinez-Sanchez M 1996 Design of a miniaturized Hall thruster for microsatellites *32nd Joint Propulsion Conference (1996, Lake Buena Vista, FL)* AIAA-96-3291
- [8] Hargus W A Jr and Cappelli M A 1998 Development of a linear Hall thruster *34th Joint Propulsion Conference (1998, Cleveland, OH)* AIAA 98-3336
- [9] Meezan N B, Hargus W A Jr and Cappelli M A 1998 Optical and electrostatic characterization of oscillatory Hall discharge behavior *34th Joint Propulsion Conference (1998, Cleveland, OH)* AIAA-98-3502
- [10] Hargus W A Jr, Meezan N B and Cappelli M A 1997 Transient behavior of a low-power laser Hall thruster *33rd Joint Propulsion Conference (1997, Seattle, WA)* AIAA-97-3050
- [11] Fife J M, Martinez-Sanchez M and Szabo J J 1997 Numerical study of low frequency discharge oscillations in Hall thrusters *33rd Joint Propulsion Conference (1997, Seattle, WA)* AIAA-97-3052
- [12] Hargus W A Jr and Cappelli M A 1998 Laser induced fluorescence measurements on a laboratory Hall thruster *34th Joint Propulsion Conference (1998, Cleveland, OH)* AIAA 98-3645
- [13] Dawson P H 1978 *J. Appl. Phys.* **37** 3644
- [14] Boeuf J P and Garrigues L 1999 *J. Appl. Phys.* **84** 3541
- [15] Meezan N B and Cappelli M A 1999 Optical emission study of anomalous electron transport in a laboratory Hall thruster *35th Joint Propulsion Conference (1999, Los Angeles, CA)* AIAA 99-2284

Appendix II

A Characterization of Plasma Fluctuations within a Hall Discharge

E. Chesta, C. Lam, N.B. Meezan, D.P. Schmidt, and M.A. Cappelli

To appear in *IEEE Transactions on Plasma Science*, 2001

A Characterization of Plasma Fluctuations within a Hall Discharge

Enrico Chesta, Cheryl Lam, Nathan B. Meezan, Dan P. Schmidt, and Mark A. Cappelli*

Thermosciences Division
Mechanical Engineering Department
Stanford University
Stanford, California 94305-3032

Abstract

Experimental results are presented for studies of low (2-20 kHz) and intermediate-frequency (20-100 kHz) oscillations in crossed-field closed-electron drift Hall discharges. Conditional sampling using two electrostatic probes is used to identify and extract properties of coherent structures associated with the propagation of azimuthal and longitudinal instabilities within the discharge channel. The azimuthal component phase velocities are determined for a wide range of wave frequencies and over characteristic regimes of operation of these devices. A variety of propagation modes are observed and analyzed, including the appearance of an induced mode due to the presence of the probes themselves. This later result is believed to be the first direct evidence of how fluctuations can be influenced in these Hall discharges using relatively simple actuation methods.

Index Terms - Hall discharges, Langmuir probes, plasma propulsion, plasma instabilities.

*Author to whom correspondence should be sent.

Submitted to IEEE Transactions on Plasma Sciences, August 2000. Revised, January 2001.

I. INTRODUCTION

Closed electron-drift Hall discharges are low-pressure ($\sim 0.01 - 0.1$ Pa), weakly collisional, magnetized plasma sources that generate a relatively high velocity ion beam suitable for use in space propulsion applications. A particular class of Hall plasma thrusters, the so-called "Stationary Plasma Thruster," has been used in a number of space missions in the former Soviet Union [1]. A variation of this Hall thruster that has an annular (co-axial) discharge channel 100 mm in diameter – the SPT-100, has a high specific impulse (1100 – 2000 sec), operates at moderately high thrust levels (55 – 150 mN), and has an exceptionally high thrust efficiency (40-60%). Because of this performance, this plasma source is now being aggressively developed for use in station keeping applications on western satellites.

In a typical co-axial geometry Hall discharge (Fig. 1), the plasma is sustained in imposed orthogonal electric and magnetic fields. The discharge electrons, a large fraction of which are emitted by an external cathode, are magnetized, whereas the more massive propellant ions, usually xenon, are not. Consequently, the electrostatic fields established by the retarded electron flow accelerate the ions to high velocities, typically 50-60% of the discharge voltage ($\sim 100-300$ V). The maximum acceleration occurs in the region between the magnetic poles, where the magnetic field is a maximum. In a co-axial geometry, the electrons are constrained to move in the closed, azimuthal $\mathbf{E} \times \mathbf{B}$ drift, with cross-field diffusion providing the necessary current to sustain the discharge. An annular ceramic channel confines the electron flow towards the anode, located at its base.

It is widely known that the Hall discharge plasmas exhibit a rich spectrum of fluctuations in plasma properties [2]. While it is not yet known if and how these fluctuations can impact the performance of a Hall thruster, it is believed that fluctuations in the bulk plasma properties are partly responsible for anomalous electron transport across the imposed magnetic field [3]. While some studies characterizing the presence and origin of these fluctuations and their possible control were published in the mid 60's to mid 70's [3-9], they have received increased attention recently [10-15], as there is a growing need to extend and enhance the performance of these thrusters for a broader range of space missions.

Our research is motivated by the possibility of enhancing Hall thruster operation by the active control of these fluctuations, or by the passive suppression of the fluctuations in regions of the discharge channel where a reduction in electron current is desired. To do so, it is important that the nature of these fluctuations is adequately understood. In this paper, we present an experimental

characterization of the propagation of these disturbances over a range of Hall discharge operation, and demonstrate that it is possible to affect the oscillations within the discharge by the insertion of biased probes.

II. EXPERIMENT

The Hall discharge plasma source used in this study is a laboratory version of a low-power Hall thruster, and is described in more detail in previous papers [16-18]. This particular source is intended to be used as a test bed for studying the discharge physics and not to serve as an operational prototype plasma accelerator, although the principal design is similar to that used in practise. The time-averaged plasma properties within the annular discharge channel have been extensively characterized for a range of operating conditions [16]. The source consists of an annular alumina channel, 90 mm in diameter, 11 mm in width, and 80 mm in length. A magnetic circuit consisting of four outer coils, one inner coil, and three iron plates provides a magnetic field (mostly radial in direction) peaked near the exit of the discharge channel, as shown in Fig. 2. The mapping of the axial and radial components of the magnetic field strength within the channel is performed with a Hall probe in the absence of the plasma. The radial component of the magnetic field is found to drop off by approximately 15% at the inner and outer walls of the acceleration channel. Details of the two-dimensional magnetic field distribution for magnet currents used here can be found in [18]. A hollow stainless steel ring with 32 holes of 0.5 mm diameter serves both as the anode and the propellant (gas) input of the discharge. A commercial hollow cathode (Ion Tech HCN-252) is used to neutralize the resulting ion beam and provide the necessary electron current to sustain the discharge. The cathode is mounted such that its exit aperture is approximately 2 cm downstream of the plasma source exit. The cathode body was kept at the vacuum chamber ground potential. During discharge operation, the 1 m diameter by 1.5 m long chamber within which the discharge was operated was maintained at a pressure of 10^{-4} Torr (uncorrected for xenon), as indicated by an ionization gauge. Flanged elbows (0.5 m in diameter) at each end of the vacuum chamber supported two 0.5 m diameter diffusion pumps, operated without baffles, for maximum pumping speed (approximately 6000 l/s).

For the measurements reported on here, the xenon flow rate was 2 mg/s and a constant solenoid winding current of 125 mA provided a peak magnetic induction of about 100 G at 5mm upstream of the exit plane (inside the channel). The characteristics of the plasma fluctuations on centerline within the channel were studied at various discharge potentials.

Plasma density fluctuations were detected by two azimuthally-placed low-impedance Langmuir probes biased negatively with respect to the plasma potential to collect the ion saturation current, with the current density given as [19]:

$$J_{is} = 0.61 \ e n_e \sqrt{\frac{k T_e}{m_i}} \quad (1)$$

Here, T_e is the electron temperature, n_e is the electron number density, m_i is the xenon ion mass, e is the electron charge, and k is the Boltzmann constant. In Eqn. 1, it is assumed that the distant plasma is quasi-neutral ($n_e = n_i$), and that the ions enter the collisionless sheath at the Bohm velocity. While the fluctuations in collected current can be a result of both fluctuations in electron density and temperature, in prior studies, it has been shown that these low frequency disturbances at low operating potential are largely isothermal [3, 7].

A schematic of the Langmuir probe construction is shown in Fig. 3. The exposed part of the probe consisted of a 0.254 mm diameter, 3 mm long tungsten wire. The base of the probe was of a complex design, intended to minimize stray capacitance for extended frequency response. The probe base consisted of an alumina tube directly surrounding the tungsten wire (0.508 mm ID, 1.27 mm OD), followed by a stainless steel tube (1.48 mm ID, 1.58 mm OD), connected to the braided ground of a 50 Ω co-axial cable. The inner tungsten wire was connected to the center pin of the co-axial cable. This outer stainless steel tubing served as a shield to isolate the extended probe base from disturbances other than at the tip of the probe. The stainless steel tubing was then surrounded by another alumina tube (1.6 mm ID, 2.3 mm OD) and the entire inside air spaces were potted with an alumina paste.

The probe size was minimized so as to reduce its overall capacitance, and for the studies reported on here, was approximately 10 cm in length. Coaxial transmission line feed-throughs provided the transfer of the probe signal through the vacuum chamber to a National Instruments DAQScope 5102 digital oscilloscope card operating at an 800 kHz sample rate. Data was stored on a personal computer for future processing. The probes were terminated with 50 Ω at the input of the oscilloscope card. In this way, the probe tips were negatively biased (close to system ground) with respect to the plasma, which is predominantly at high positive potential, since the anode is maintained at a minimum of 86V, and since the near exit plane potential is always greater than 40V due to the cathode fall and finite electron temperature. Occasional scans of the Langmuir probe

across the electron retarding regime to regions of high negative bias verified that system ground potential was always in the ion current saturation regime.

The probes were oriented such that the exposed center wire axis was parallel to the axial coordinate of the thruster, and placed midway between the inner and outer insulating walls, as illustrated in Fig.4. Probe translation along the axial direction (the direction of the annular channel) was provided by a translation stage driven by a Slo-Syn stepper motor, powered and controlled by a Compumotor model SX Microstepping Drive/Indexer System. The azimuthal positions of the two probes were manually set before the beginning of each experiment, maintaining an equal angular distance from the two nearest outer magnetic coils. For this study, probe separations between 30 and 180 degrees were examined. In most cases, the axial probe locations varied between a distance of approximately 35 mm from the anode ($x = -45$ mm) and 10 mm beyond the exit plane ($x = 10$ mm), with the $x = 0$ reference taken to be the exit plane of the discharge, and negative positions implying that the probe locations are inside the discharge channel.

A fast Fourier transform of the signal from each probe was performed across a temporal window that was 1.25 msec wide and spaced every 0.625 msec in time. This operation was used to convert the digital signal in the time domain into the frequency domain, for every temporal interval, over the length of the temporal data set (in some cases, 0.625 sec long). To study the fluctuating component to the signals, the mean signal was removed (numerically) from the transient signal prior to its processing. A comparison of the mean signals, and the power spectrum from each of the two probes verified that the probes had equal sensitivities (to within $\sim 10\%$) and frequency responses. To avoid aliasing, only frequencies below 400 kHz (the Nyquist frequency, defined by the 800 kHz sampling rate used for all of the studies described here) were considered for interpretation. In the future, higher sampling rates will be used to better explore higher instability frequencies, since most of the probes used here were found to have a 20dB cut-off of well beyond 1 MHz.

Typical current (I) – voltage (V) discharge characteristics, as monitored by digital multi-meters, for the flow rates and magnetic field strength used for these studies is shown in Fig. 5. In some cases, these mean values were verified by recording the discharge current oscillations with a differential amplifier placed across a 4-ohm ballast resistor in the anode circuit. At the higher discharge voltages (e.g., ~ 200 V), the probes were seen to clearly affect the mean discharge current, perturbing it by as much as 20-30%. During the collection of the data, the residence time of the probes within the channel was several minutes. Damage to the probes from ion bombardment

precluded the collection of data beyond approximately 185V. While it is difficult to say how the immersion of the probes into the plasma affected the spontaneous instabilities detected, we discuss later in the paper the clear presence of waves that are induced by the presence of the probes themselves within the discharge channel.

III. DATA ANALYSIS

The data collected by a single probe was cast to display three-dimensional renderings of the plasma density fluctuations, as shown in Figs. 6 and 7. The axial variation in the mean electron density for three operating conditions has been reported previously [16], and is provided again here for reference (Fig. 8). In Fig. 6, the amplitude of the plasma density fluctuations are displayed verses operating voltage, for four axial locations $x = 12.7$ mm, 0 mm, -12.7 mm, and -25.4 mm. Prominent in these figures is the presence of strong, relatively low frequency disturbances in the range of 5 – 30 kHz, and a broader range of disturbances towards higher frequencies, at very low voltages downstream of and at the exit plane, and at high voltages upstream of the exit plane. Similar spectral maps have been reported for the behavior of discharge current oscillations in the Russian Stationary Plasma Thruster SPT-70 [15].

In Fig. 7, the Fourier component amplitudes of the plasma density fluctuations and the ratios of the amplitudes to the mean are displayed verses axial position for a range of operating voltages. We find that the fluctuations in the plasma density can be as high as the mean values. While it is apparent that the fluctuations are most intense near the exit plane, it is noteworthy that the relative fluctuations (amplitude of the fluctuations divided by the mean value) actually diminish in the region between $x = -20$ mm and $x = 0$ mm over a wide range of operating conditions. Note also that the broadband fluctuations are concentrated at $x = -10$ mm and beyond the exit plane at low voltages, but are damped in this spatial region at high voltages. This dramatic difference suggests that the nature of these high frequency disturbances differ depending on the operating voltage.

A comparison of the response of two probes located at the same axial position, but separated by some angle on the azimuth, provides additional information on the nature of these disturbances. A cross-spectral analysis of the signals from the two probes provides a measure of their coherence, suggests the direction of propagation, and can be used to estimate the azimuthal phase velocity. The azimuthal phase velocity V_{py} of the disturbances can be obtained from:

$$V_{py}(f) = 2\pi f \left(\frac{\theta_p R}{\phi_2(f) - \phi_1(f)} \right) \quad (2)$$

where θ_p is the angular probe separation (in radians), R is the channel radius, $f = \omega/2\pi$ is the frequency, and $\phi_{1,2}$ are the phase shifts of the individual probe signals, determined from:

$$\phi_{1,2}(f) = \tan^{-1} \left(\frac{\text{Im}_{1,2}(f)}{\text{Re}_{1,2}(f)} \right) \quad (3)$$

with Re and Im the real and imaginary components of the complex Fourier transform $F(f) = \text{Re}(f) + i\text{Im}(f)$, respectively.

The signals from the two probes were used to derive wave dispersion maps, rendered as the phase velocity verses wave frequency. In all cases, conditional sampling is employed, to isolate only the strongest correlated disturbances detected by the two probes. Two examples of dispersion maps are shown in Fig. 9, for a relatively low operating voltage (100V) and an axial position of $x = 0$, and for a relatively high voltage (172V) and a location just 12 mm beyond the exit plane. For these dispersion studies, the azimuthal probe separation was $\theta_p = 30^\circ$. Disturbances were considered only if the amplitude of the component on the first probe was at least three times its mean, and that on the second probe, within its mean and five times its mean. The condition imposed on the second probe allows for the possible damping of the wave or loss of intensity due to out-of-plane propagation.

Also drawn in the dispersion maps of Fig. 9 are lines corresponding to the azimuthal component phase velocities for the $m=1$, $m=4$, and $m=12$ azimuthal modes of the cylindrical annulus. In general, we can express the azimuthal phase velocity for a tilted azimuthal mode:

$$V_{py} = \frac{2\pi \cos(\alpha)}{\sqrt{k_x^2 + k_y^2}} \cdot f = \frac{2\pi \cos(\alpha)}{\sqrt{k_x^2 + \left(\frac{m}{r}\right)^2}} \cdot f \quad (4)$$

Here, k_x and k_y are the component wavenumbers along the axial and azimuthal directions, respectively. We assume that $k_y = m/r$, and m is the integer azimuthal mode number. For a purely azimuthal wave, the axial wave number component is $k_x = 0$. For $m = 1$ and $k_x = 0$ condition, the oscillation wavelength is equal to the channel circumference, $2\pi r$ where as it is one-fourth and one-twelfth the circumference for the pure azimuthal $m = 4$ and $m = 12$ modes, respectively. In the top

frame of Fig. 9, we also depict vertical lines corresponding to possible $m = 0$ modes. For $m = 0$, the wave is longitudinal and the azimuthal phase velocity is infinite. In general, the observed natural disturbances can have both azimuthal and axial components, and can propagate with an angle α , defined by:

$$\tan \alpha = \frac{k_x}{k_y} \quad (5)$$

An examination of the dispersion maps, and comparison to the lines associated with the pure azimuthal $m = 1$ mode suggests that some of these disturbances may be tilted out of the azimuthal plane (ie $k_x \neq 0$). Indeed, for the $m = 1$ modes shown in the top and bottom frames of Fig. 9, a propagation angle of 15° and 20° respectively has been used to best capture the trends seen for these disturbances. The strong $m = 1$ low-frequency disturbances at $x = 0$ also appear, however, to have a range in the possible propagation directions, preferring lower propagation angles at the lower frequencies.

IV. RESULTS DISCUSSION

A number of features are identifiable in the dispersion maps of Fig. 9, attributed here to four or possibly five intrinsic instabilities, and an instability induced by the probes themselves. We shall discuss them here, some within the context of what has been seen experimentally in previous Hall discharge studies.

The most prominent mode seen at low voltages is that of a relatively strong, $m = 1$ azimuthally propagating disturbance of frequency in the 5-10 kHz range, and of phase velocity $V_{py} \sim 1000 - 4000$ m/s, nearly equal to the critical ionization velocity of the xenon propellant. As mentioned above, that the data in this region departs slightly from the superimposed line $m = 1$ ($\alpha = 15^\circ$) line suggests that this disturbance lacks a unique tilt in its propagation vector, and that the propagation angle tends to increase slightly with increasing frequency. These waves are similar in their properties to those identified by Janes and Lowder [3], and others [4,7], as “rotating spokes”, and are attributed to tilted ionization waves of still unknown origin, although the connection to the critical ionization velocity may be more than coincidental since an appropriate scaling is found when operating on different inert gases [3]. A second prominent mode seen at low discharge voltage is that associated with nearly purely $m = 0$ axial modes at higher frequencies, a few of which are identified on the figure by superimposing vertical lines at characteristic frequencies. These modes will be more apparent on

dispersion plots discussed later. While the behavior of these modes are consistent with an $m = 0$ azimuthal mode, they could be higher-order azimuthal modes that are propagating in the axial direction (the azimuthally spaced probes would not resolve this). These high frequency modes correspond to the nearly constant frequency bursts seen as intense horizontal striations in the low voltage (86V and 100V) spectral maps in Fig. 7. It is noteworthy that these disturbances are relatively turbulent and broadband, and they exhibit a curious power-law behavior in their spectral distribution. Fig. 10 displays the Fourier transform of the plasma density fluctuations for the 100V and also 86V cases, showing a characteristic $-5/3$ power law power-law decay in the amplitudes at frequencies beyond 20 kHz (indicated by the dashed line in the figures). It is natural at first to suspect that these turbulent, longitudinal disturbances may correspond to the so-called "transit time" oscillations first identified by Morizov and colleagues [4,7], and conjectured to be associated with transit time of ions within the acceleration channel. We dismiss this possibility here, because we see that they are excited at relatively low discharge voltage (in the ionization branch of the I-V characteristic), unlike the broadband oscillations described in Ref. 4 and 7. Furthermore, the frequencies are much lower than the inverse transit time of the ions in the acceleration region of the thruster, which, for our case, is approximately 500 kHz.

A third mode seen in the low discharge voltage dispersion plot in Fig. 9 appears actually as a low-velocity cut-off to the higher frequency longitudinal modes, and is identified on the frame with a line corresponding to an $m = 4$ mode. The origin of this clear demarcation is not presently understood, although we suspect that it is associated with an azimuthal asymmetry due to the four equally spaced magnetic solenoids that connect to the front outer pole-piece. The persistence of this demarcation is seen to weaken with increasing voltage, and is non-existent at the higher discharge voltages studied. This result is consistent with an examination of the axial and azimuthal variation in the mean signal from a single probe, which reflects the spatial variation in mean plasma density, as seen in Fig. 11 for a representative low voltage (86V) and high voltage (150V) condition. It is seen that the four-fold asymmetry associated with the solenoid placement is more apparent in the azimuthal variation in the plasma density at lower voltages. The interaction between the axial disturbances and the $m = 4$ azimuthal asymmetry is the subject of ongoing research in our laboratory.

A fourth mode which appears at high operating voltages is that of an azimuthal $m = 1$ wave, tilted to approximately 20° , and in the frequency range above 20 kHz (see Fig. 9 panel for 172V

condition). High frequency azimuthal disturbances (extending as far as ~ 1 MHz) have been identified in the past [8] and have been attributed to drift instabilities of “magnetosonic” waves, excited primarily in the axial region where the magnetic field gradients have negative values (i.e., B decreases with increasing distance from the anode). Simple theories have been suggested for the growth rate and the dispersion of these waves [8] based on a multi-fluid description of the magnetohydrodynamic flow, although a rigorous comparison to experimental measurements has not yet been carried out. While it is tempting to suggest that the disturbances at low frequencies seen here may be the band edge of such drift-instabilities, our results do not support such an assignment, since these azimuthal waves, responsible for the high frequency disturbances shown in Fig. 7 (for the high voltage conditions) are not largely excited in the region of negative magnetic field gradients. In fact, there is a sudden damping of the waves at approximately $x = -5$ mm, beyond which there is very little high frequency activity. This location, which defines the edge of the activity of these disturbances, is about the location of the peak in the magnetic field (see Fig. 2). It is also tempting to suggest that the azimuthal disturbances seen at higher discharge voltages may simply be an extension of the low frequency azimuthal waves seen at lower voltage. However, the azimuthal waves seen at the lower voltages are predominantly excited in regions where the magnetic field gradients are negative, consistent with what has been seen in the literature [4].

A fifth mode that is apparent at high voltage conditions is that of an exceptionally strong low-frequency (~ 5 -10 kHz) axial ($m = 0$) disturbance that is present within the ionization zone. This disturbance, which is associated with very strong overall discharge current fluctuations, is known to interact with the external circuitry driving the discharge [20]. In the literature, this instability has been referred to as the characteristic “breathing” mode [20], the “circuit” instability [2], or the “loop” instability [9]. The origin of this instability is now reasonably well understood and its behavior has been captured in many discharge simulations [21-23]. The instability is characteristic of a predator-prey behavior in the neutral xenon and xenon ion dynamics, coupled by the ionization process [22]. It is manifested as a disturbance in the balance between the rapid removal of xenon ions within the discharge channel via electrostatic acceleration, and the replenishment of the channel with ions created from the slow-moving neutrals. The characteristic frequency of this instability is expected to be close to the inverse of the residence time of the neutrals within the ionization zone, and has been found to scale appropriately with diminishing discharge scale lengths [24].

A sixth mode that is identifiable in both frames of Fig. 9 is that of an $m = 12$ azimuthal wave, which has a wavelength equal to that of the separation between the two probes, and is believed to be “anchored” by the placement of the probes within the discharge annulus. The mode number of these disturbances is found to track the relative placement of the two probes used to study the intrinsic plasma fluctuations, as shown in Fig. 12, for exit plane disturbances ($x = 0$ mm), and a moderate operating voltage (125V). An intriguing feature of the plots in Fig. 11 is that the placement of the probes also impacts the behavior of the other prominent $m = 1$ mode. It is noteworthy that as the mode number corresponding to the separation of the probes diminishes, there seems to be an increased “coupling” of the disturbances, as seen by the tendency of the points on the $m = 1$ line to “gravitate” towards the line corresponding to the dispersion of the induced modes. The discovery of this induced perturbation and the coupling of these disturbances to the $m = 1$ mode may have applications in the control of thruster oscillations, and, quite possibly, the control of electron transport if strongly correlated azimuthal waves are largely responsible for the anomalous axial electron flow.

Fig. 13 gives the dispersion plots obtained for some of the operating conditions of the spectral maps shown in Fig. 7. A comparison is made between the plots obtained at three axial locations. At an axial location corresponding to the exit plane of the discharge ($x = 0$), we see that high discharge voltage operation is dominated by relatively strong high frequency $m = 1$ azimuthal waves (tilted slightly with respect to the azimuthal plane), and low frequency longitudinal waves, most likely associated with the “breathing” mode ionization instability. At lower voltages, the high frequency azimuthal waves become apparently more longitudinal in direction, and there is a growth of very strong low-frequency azimuthal waves, associated with the ionization process. For the low voltage case shown, the azimuthal asymmetry associated with the placement and separation of the magnetic solenoids plays a significant role in the wave dynamics only beyond $x = 0$ mm, and appears to have a dominating effect on the propagation of the disturbances in this region. A comparison of the dispersion plots at the three locations for the highest operating voltage shown confirms the conclusions that were drawn earlier that the growth and propagation of these higher frequency azimuthal waves do not depend on the sign of the local gradient in the magnetic field in contradiction to what has been postulated in the literature for azimuthal waves of higher frequency [4,7]. On the other hand, a comparison of the dispersion plots for these three axial locations for the lowest

operating voltage shown suggests that the low-frequency azimuthal waves indeed are seen to be active most notably in the region where the magnetic field gradients are negative.

V. SUMMARY

A detailed examination of the propagation behavior of low (2-20 kHz) and intermediate-frequency (20-100 kHz) oscillations in closed-electron drift Hall a discharge is presented. Conditional sampling using two electrostatic probes collecting ion saturation current is used to identify and extract properties of correlated structures associated with the propagation of azimuthal and longitudinal instabilities within the discharge channel. The azimuthal component phase velocities (dispersion plots) are determined for a range of wave frequencies and over characteristic regimes of operation of the discharge. A variety of propagation modes are observed and analyzed, some of which have been documented in the previous literature. In addition to the low-frequency azimuthal "spokes" and the so-called "breathing mode" that is well known to be excited in these discharges, we have identified the appearance longitudinal disturbances (that are prevalent at low discharge voltages) and azimuthal disturbances (at higher discharge voltages) in the 20 – 100 kHz range that do not seem to have been described previously. Finally, we have seen that the presence of azimuthal non-uniformities due to the location of the magnetic solenoids, and, due to the placement of the diagnostic probes, can couple strongly to the intrinsic natural instabilities. Such methods of coupling to the natural dynamical behavior of these discharges may be useful in the control or enhancement of turbulence, which is known to influence the axial electron transport.

Acknowledgements

This research was funded by the Air force Office of Scientific Research. N.B. Meezan was supported through a National Defense Science and Engineering Graduate Fellowship. Additional support for E. Chesta was provided by the Politecnico di Torino, Italy, and by the Ecole Centrale Paris, France, through the Top Industrial Managers for Europe program.

References

- [1] G.A. Popov and Y.A. Ryzhov, "Electric propulsion in Russia and its practical applications", *Z. Flugwiss. Weltraumforsch* **17**, 161-169, 1993.
- [2] E.Y. Choueiri, "Characterization of oscillations in closed drift thrusters", AIAA Paper No. 94-3013, 30th Joint Propulsion Conference, Indianapolis, IN, June 27-29, 1994.

- [3] G.S. Janes and R.S. Lowder, "Anomalous electron diffusion and ion acceleration in a low-density plasma", *Phys. Fluids* **9**, 1115-1123, 1966.
- [4] A.I. Morozov, Y.V. Esipchuk, A.M. Kapulkin, V.A. Nevrovskii, and V.A. Smirnov, "Effect of the magnetic field on a closed-electron-drift accelerator", *Sov. Phys. – Tech. Phys.* **17**, pp. 482-487, 1972.
- [5] A.I. Morozov, V.A. Nevrovskii, and V.A. Smirnov, "Effect of feedback system on the plasma flux in an accelerator with closed electron drift", *Sov. Phys. – Tech. Phys.* **18**, pp. 344-347, 1973.
- [6] A.I. Morozov, V.A. Nevrovskii, and V.A. Smirnov, "Driven electrostatic plasma oscillations in a closed electron drift accelerator", *Sov. Phys. – Tech. Phys.* **18**, pp. 339-343, 1973.
- [7] Y.V. Esipchuk, A.I. Morozov, G.N. Tilinin, A.V. Trofimov, "Plasma oscillations in closed-drift accelerators with an extended acceleration zone", *Sov. Phys. – Tech. Phys.* **43**, pp. 1466-1473, 1973.
- [8] Y.V. Esipchuk and G.N. Tilinin, "Drift instability in a Hall-current plasma accelerator", *Sov. Phys. – Tech. Phys.* **21**, pp. 417-423, 1976.
- [9] G.N. Tilinin, "High-frequency plasma waves in a Hall accelerator with an extended acceleration zone", *Sov. Phys. – Tech. Phys.* **22**, pp. 974-978, 1977.
- [10] V.I. Baranov, Y.S. Nazarenko, V.A. Petrosov, A.I. Vasin, and Y.M. Yashnov, "Electron drift oscillations outside the accelerator with closed electron drift," IEPC Paper No. 95-062, 24th International Electric Propulsion Conference, Moscow, Russia, 1995.
- [11] V.I. Baranov, Y.S. Nazarenko, V.A. Petrosov, A.I. Vasin, and Y.M. Yashnov, "Electron drift oscillations outside the accelerator with closed electron drift," AIAA Paper No. 96-3192, 32nd Joint Propulsion Conference, Lake Buena Vista, FL, July 1-3, 1996.
- [12] D. Kusamoto and K. Komurasaki, "Optical diagnostics of the plasma in the channel of a Hall thruster" IEPC Paper No. 97-067, 25th International Electric Propulsion Conference, Cleveland, OH, 1997.
- [13] F. Darnon, M. Lyszyk, and A. Bouchoule, "Optical investigations on plasma oscillations of SPT thrusters," AIAA Paper No. 97-3051, 33rd Joint Propulsion Conference, Seattle, WA, July 6-9, 1997.

- [14] M.A. Cappelli, W.A. Hargus, Jr., and N.B. Meezan, "Coherent structures in crossed-field closed-drift Hall thrusters," IEEE Trans. Plasma Sciences **27**, pp. 96-97, 1999.
- [15] N. Gascon, C. Perot, G. Bonhomme, X. Caron, S. Bechu, P. Lasgorceix, B. Izrar, M. Dudeck, "Signal processing and non-linear behavior of a stationary plasma thruster: first results", AIAA Paper No. 99-2427, 35th Joint Propulsion Conference, Los Angeles, CA, June 20-24, 1999.
- [16] N.B. Meezan and M.A. Cappelli, "The anomalous electron mobility in a coaxial Hall discharge plasma" *submitted to Physical Review E*, June, 2000.
- [17] W.A. Hargus, Jr., and M.A. Cappelli, "Laser induced fluorescence measurements on a laboratory Hall thruster," AIAA Paper No. 98-3645, 34th Joint Propulsion Conference, Cleveland, OH, July 13-15, 1998.
- [18] W.A. Hargus, Jr., "Investigation of the plasma acceleration mechanism within a co-axial Hall thruster." Ph.D. Thesis, Mechanical Engineering Department, Stanford University.
- [19] M.Lieberman and A. Lichtenberg, Principles of Plasma Discharges and Material Processing, p. 161, Wiley and Sons, NY, 1994.
- [20] V. Zhurin, J. Kahn, H. Kaufman, K. Kozubsky, and M. Day, "Dynamic characteristics of closed drift thrusters, IEPC Paper No. 93-095, 23rd International Electric Propulsion Conference, Seattle, WA, 1993.
- [21] J. P. Boeuf and L. Garrigues, "Low frequency oscillations in a stationary plasma thruster." J. Appl. Phys. **84**, pp. 3541-3554, 1998.
- [22] J. Fife and M. Martinez-Sanchez, and J. Szabo, "A numerical study of low frequency discharge oscillations in Hall thrusters," AIAA Paper No. 97-3052, 33rd Joint Propulsion Conference, Seattle, WA, July 6-9, 1997.
- [23] E. Fernandez, M.A. Cappelli, and K. Mahesh, "2D simulations of Hall thrusters", Annual Research Briefs of the Center for Turbulence Research, Stanford University, pp. 81 – 90, 1998.
- [24] D.P. Schmidt, N.B. Meezan, W.A. Hargus, Jr., and M.A. Cappelli, "A low-power, linear-geometry Hall plasma source with an open electron-drift", Plasma Sources Sci. Technol. **9** pp. 68-76, 2000.

Figure Captions

FIG. 1. Schematic of a typical Hall discharge.

FIG. 2. Axial profile of radial magnetic field strength for the Hall discharge studied.

FIG. 3. Schematic of the Langmuir probes used to detect plasma density fluctuations.

FIG. 4. Schematic of the experimental arrangement showing the location and orientation of the Langmuir probes.

FIG. 5. Typical current – voltage Hall discharge characteristics.

FIG. 6. Spectral maps of the amplitude of the fluctuations in the probe signals over discharge voltage for axial locations of 12.7 mm, 0, -12.7 mm, and -25.4 mm (top to bottom).

FIG. 7. Spectral maps of the amplitude fluctuations in probe signal (left) and ratio of the amplitude fluctuations to the mean signal (right) for discharge conditions of 86V, 100V, 128V, 161V and 184V (top to bottom).

FIG. 8. Axial variation in the mean electron density [16].

FIG. 9. Typical experimental dispersion plots derived from the azimuthal probes located at the discharge exit ($x = 0$ mm) but separated by 30° . The top frame is for a discharge voltage of 100V, and the bottom frame is for a discharge voltage of 172V.

FIG. 10. Fourier spectrum of the fluctuations in plasma density at the exit of the Hall discharge. The top frame is for a discharge voltage of 86V, and the bottom frame is for a discharge voltage of 100V.

FIG. 11. Axial and azimuthal variation in the mean plasma density for 86V and 150V operating conditions. The gray scale is such that white corresponds to peak plasma densities of approximately $3 \times 10^{17} \text{ m}^{-3}$.

FIG. 12. Dispersion plots obtained using (top to bottom) probe separations of 180, 120, 90, and 60, degrees.

FIG. 13. Dispersion maps for the discharge conditions of Fig. 6, for just two voltage conditions (128V – top panels, and 186V – bottom panels) with the probes located at $x = -12.7$ mm (left panels), $x = 0$ mm (center panels), and $x = 12.7$ mm (right panels). The dashed line (---) corresponds to the pure $m = 12$ azimuthal mode, the dotted line (...) to the $m = 1$ azimuthal mode, the dot-dash line (vertical line) to the $m = 0$ mode, and the solid line to the $m = 4$ azimuthal mode.

Figure Captions

FIG. 1. Schematic of a typical Hall discharge.

FIG. 2. Axial profile of radial magnetic field strength for the Hall discharge studied.

FIG. 3. Schematic of the Langmuir probes used to detect plasma density fluctuations.

FIG. 4. Schematic of the experimental arrangement showing the location and orientation of the Langmuir probes.

FIG. 5. Typical current – voltage Hall discharge characteristics.

FIG. 6. Frequency maps of fluctuations in the probe signals over discharge voltage for axial locations of 12.7 mm, 0, -12.7 mm, and -25.4 mm (top to bottom).

FIG. 7. Spectral maps of the amplitude fluctuations in probe signal (left) and ratio of the amplitude fluctuations to the mean signal (right) for discharge conditions of 86V, 100V, 128V, 161V and 184V (top to bottom).

FIG. 8. Axial variation in the mean electron density [16].

FIG. 9. Typical experimental dispersion plots derived from the azimuthal probes located at the discharge exit ($x = 0$ mm) but separated by 30° . The top frame is for a discharge voltage of 100V, and the bottom frame is for a discharge voltage of 172V.

FIG. 10. Fourier spectrum of the fluctuations in plasma density at the exit of the Hall discharge. The top frame is for a discharge voltage of 86V, and the bottom frame is for a discharge voltage of 100V.

FIG. 11. Axial and azimuthal variation in the mean plasma density for 86V and 150V operating conditions. The gray scale is such that white corresponds to peak plasma densities of approximately $3 \times 10^{17} \text{ m}^{-3}$.

FIG. 12. Dispersion plots obtained using (top to bottom) probe separations of 180, 120, 90, and 60, degrees.

FIG. 13. Dispersion maps for the discharge conditions of Fig.6, for just two voltage conditions (128V – top panels, and 186V – bottom panels) with the probes located at $x = -12.7$ mm (left panels), $x = 0$ mm (center panels), and $x = 12.7$ mm (right panels). The dashed line (---) corresponds to the pure $m = 12$ azimuthal mode, the dotted line (...) to the $m = 1$ azimuthal mode, the dot-dash line (vertical line) to the $m = 0$ mode, and the solid line to the $m = 4$ azimuthal mode.

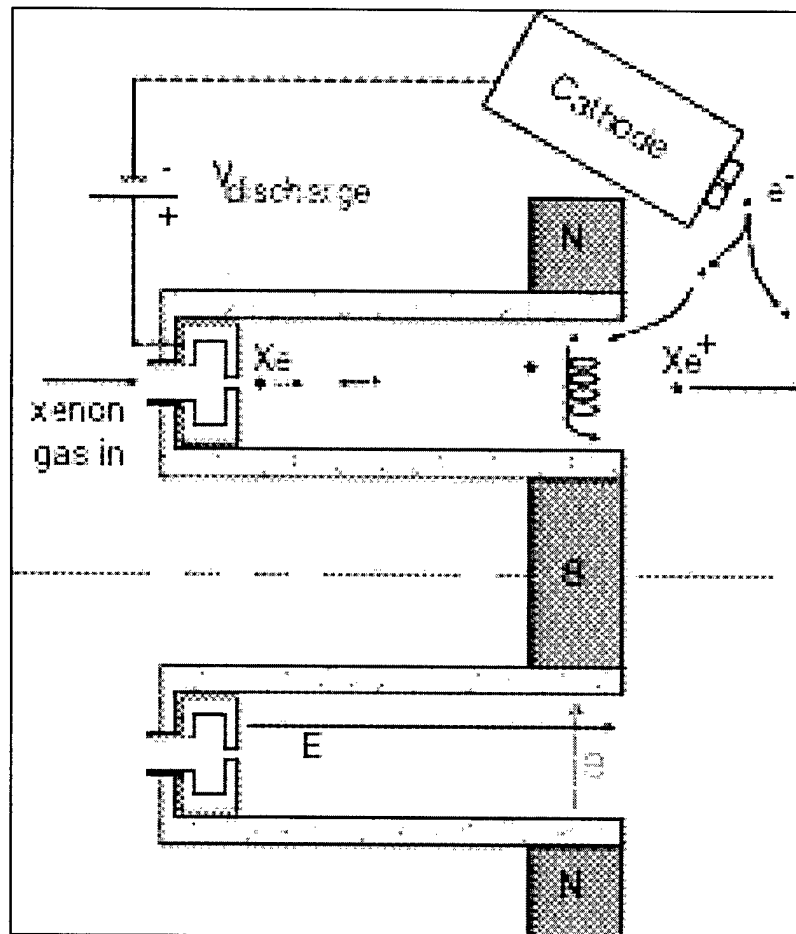


Figure 1, Chesta et al.

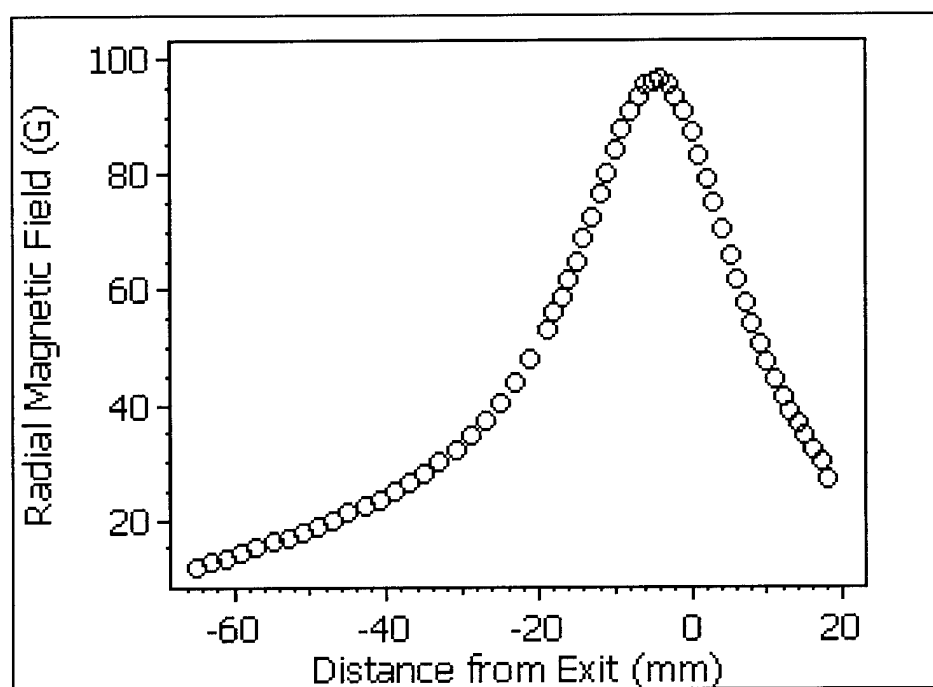


Figure 2, Chesta et al.

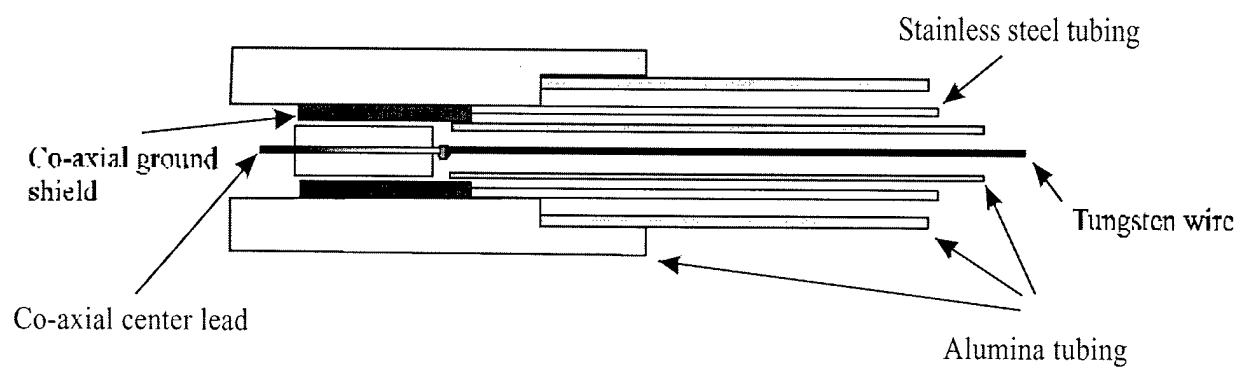


Figure 3, Chesta et al.

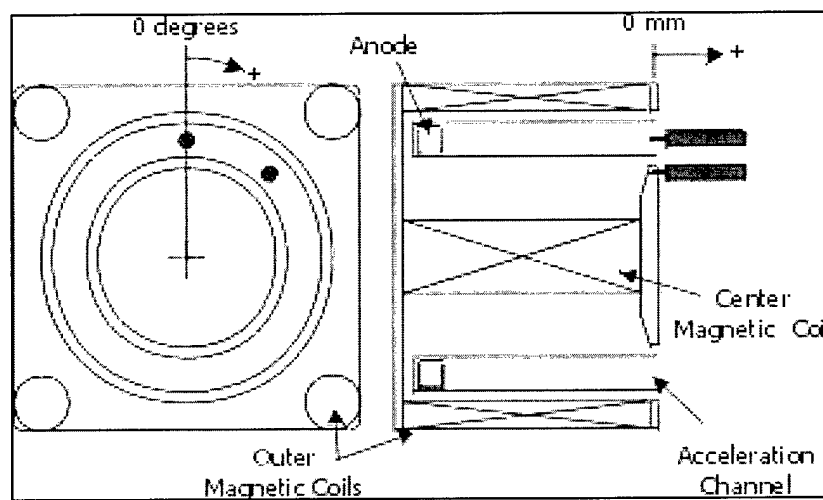


Figure 4, Chesta et al.

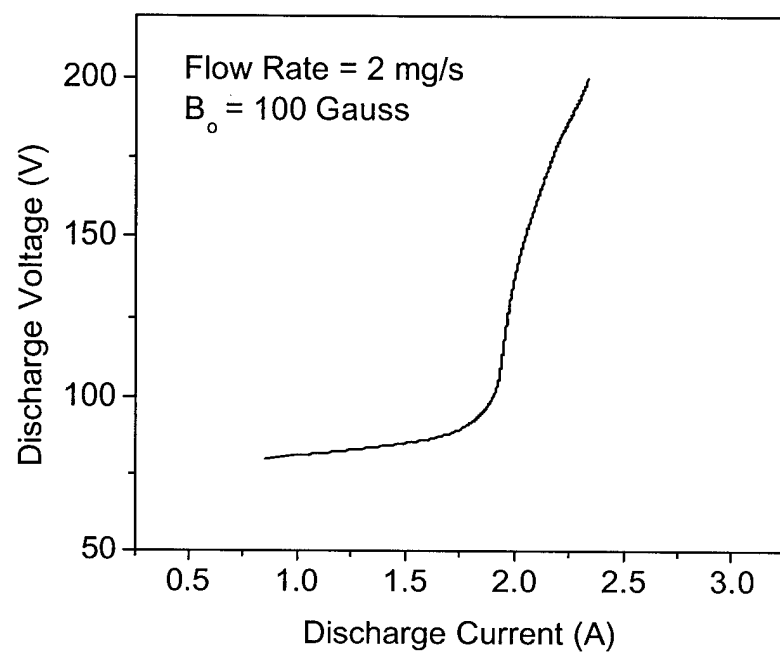


Figure 5, Chesta et al.

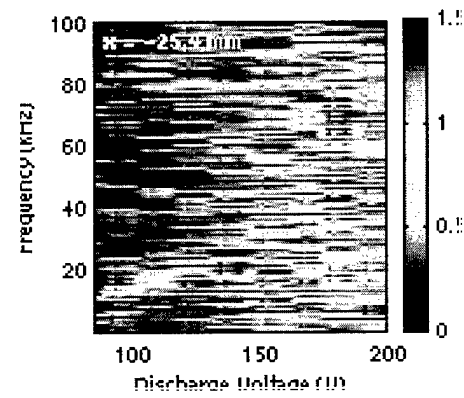
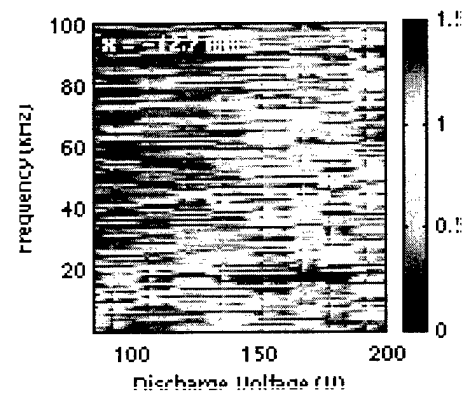
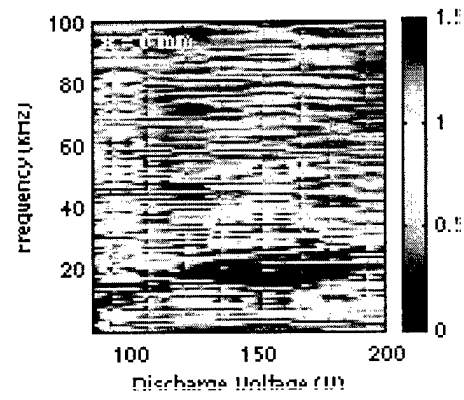
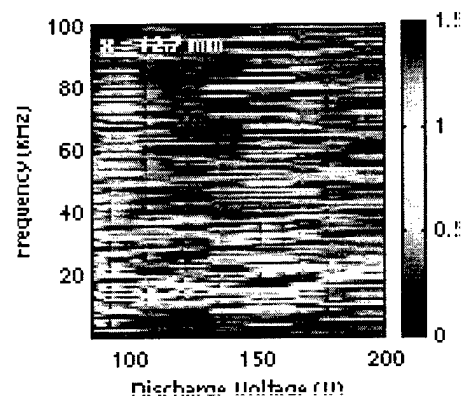


Figure 6, Chesta et al.

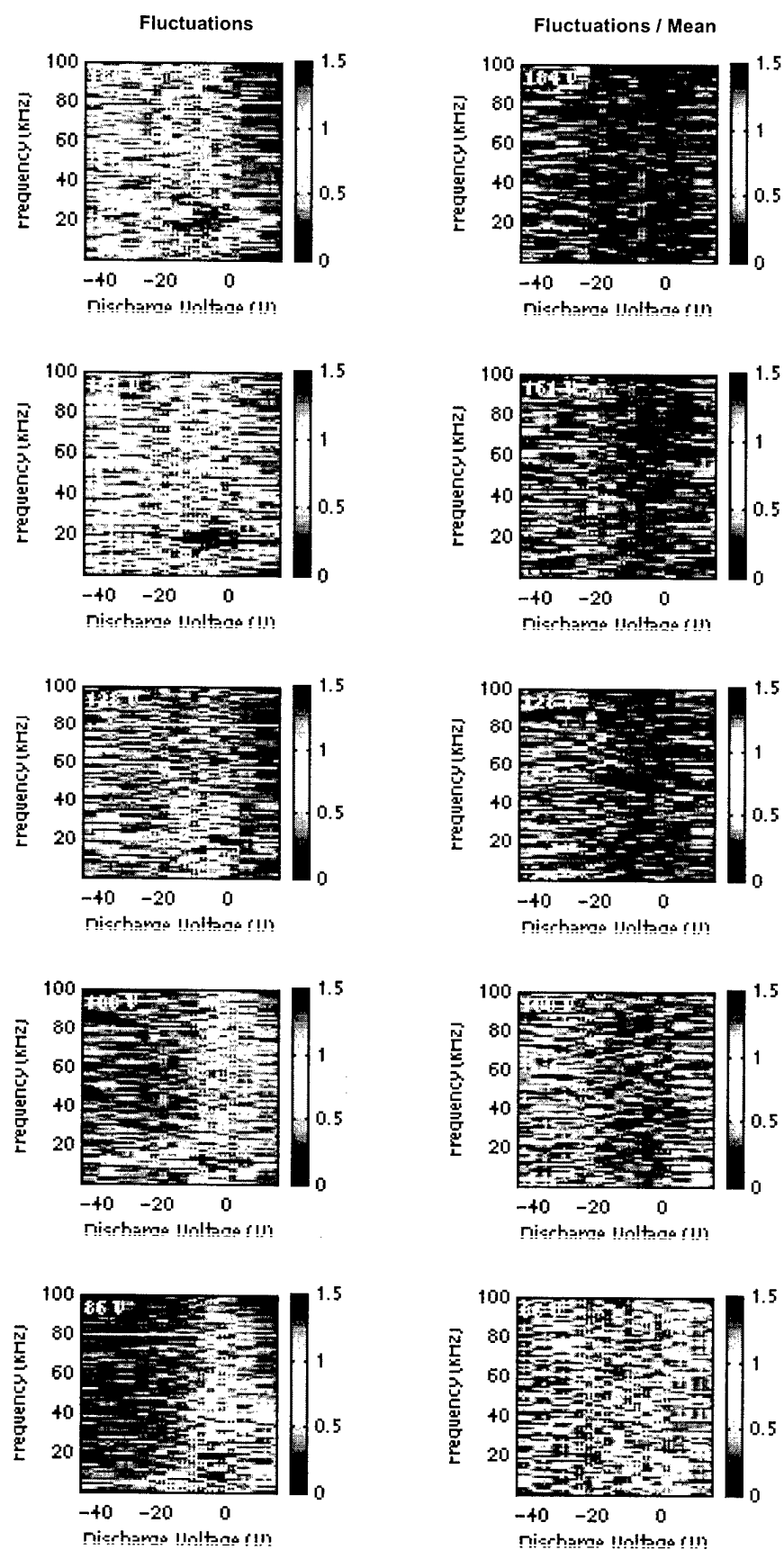


Figure 7, Chesta et al.

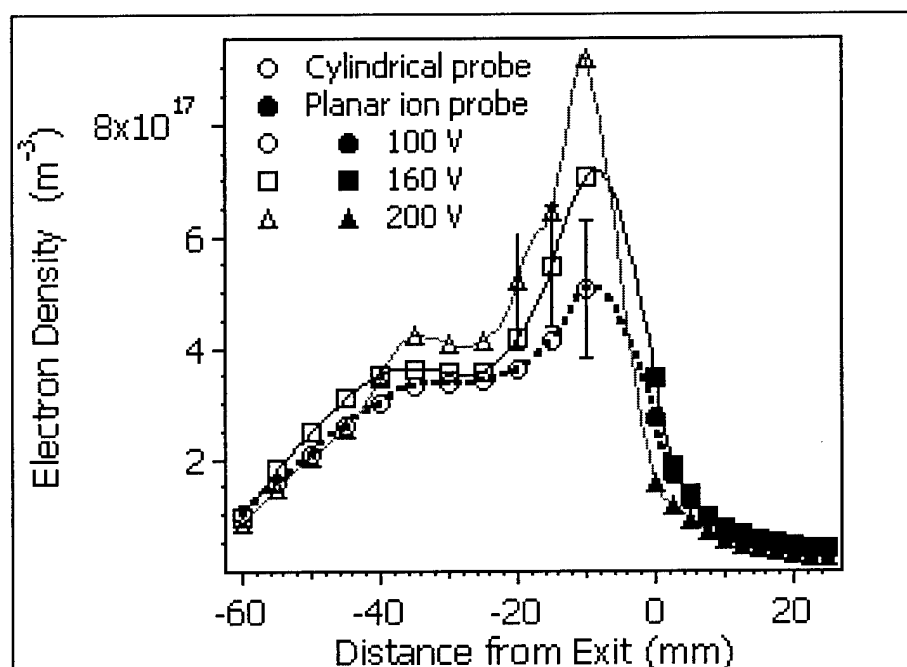


Figure 8. Chesta et al.

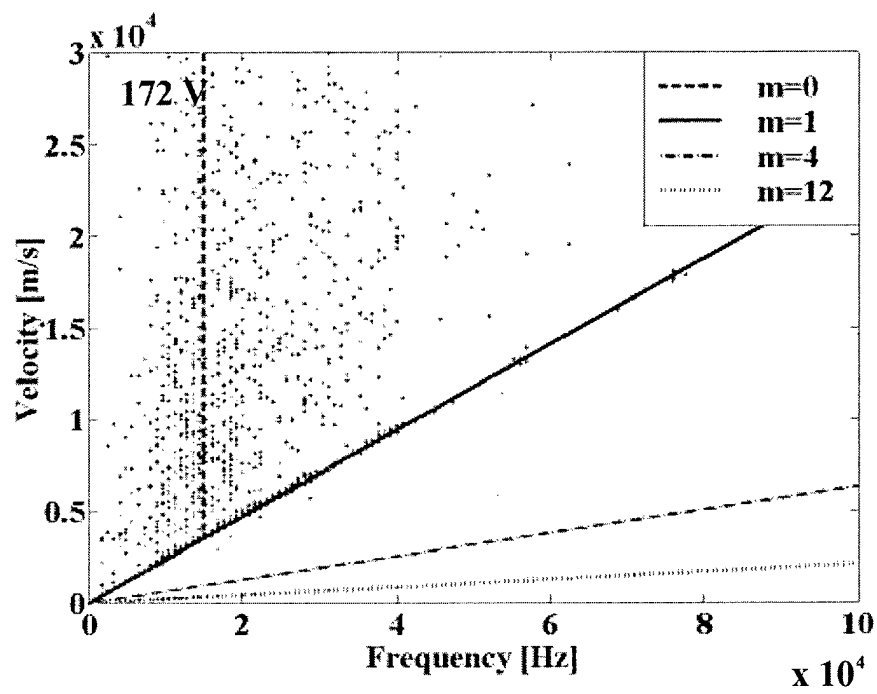
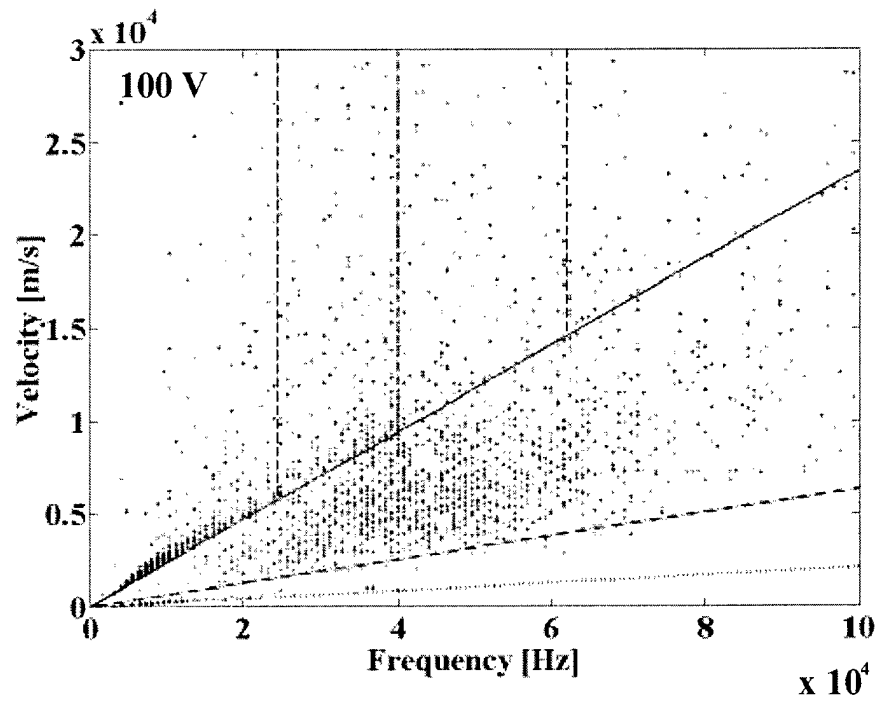


Figure 9. Chesta et al.

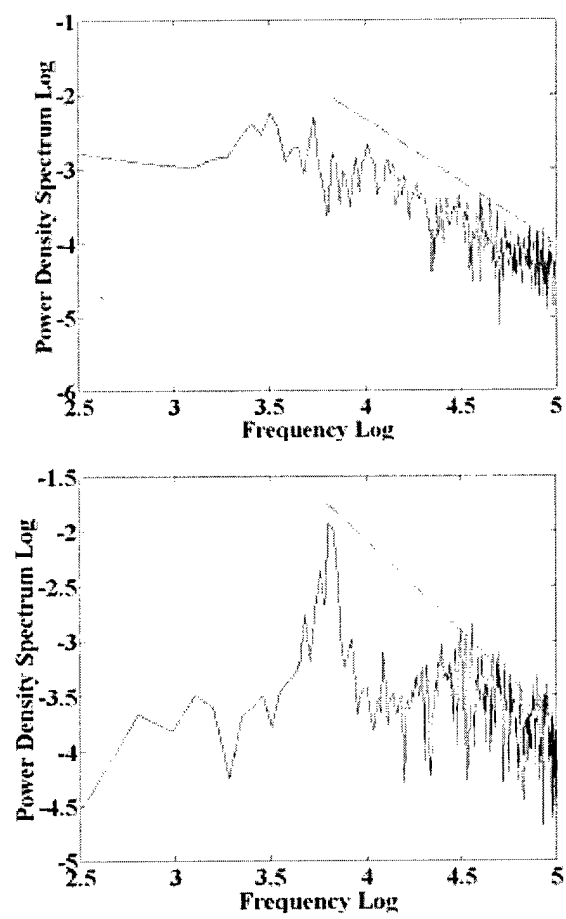


Figure 10. Chesta et al.

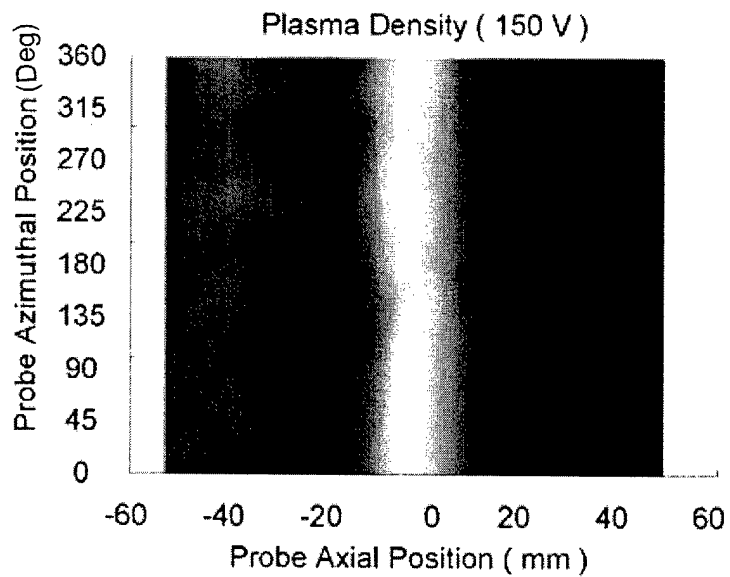
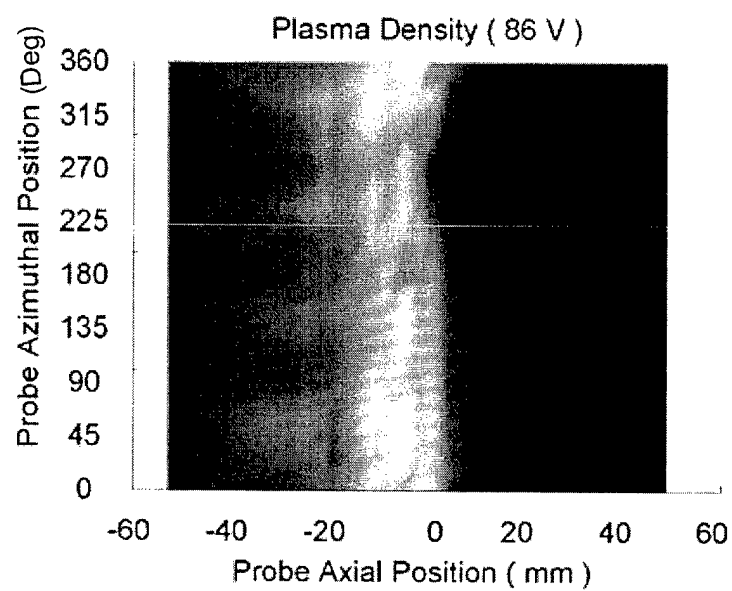


Figure 11. Chesta et al.

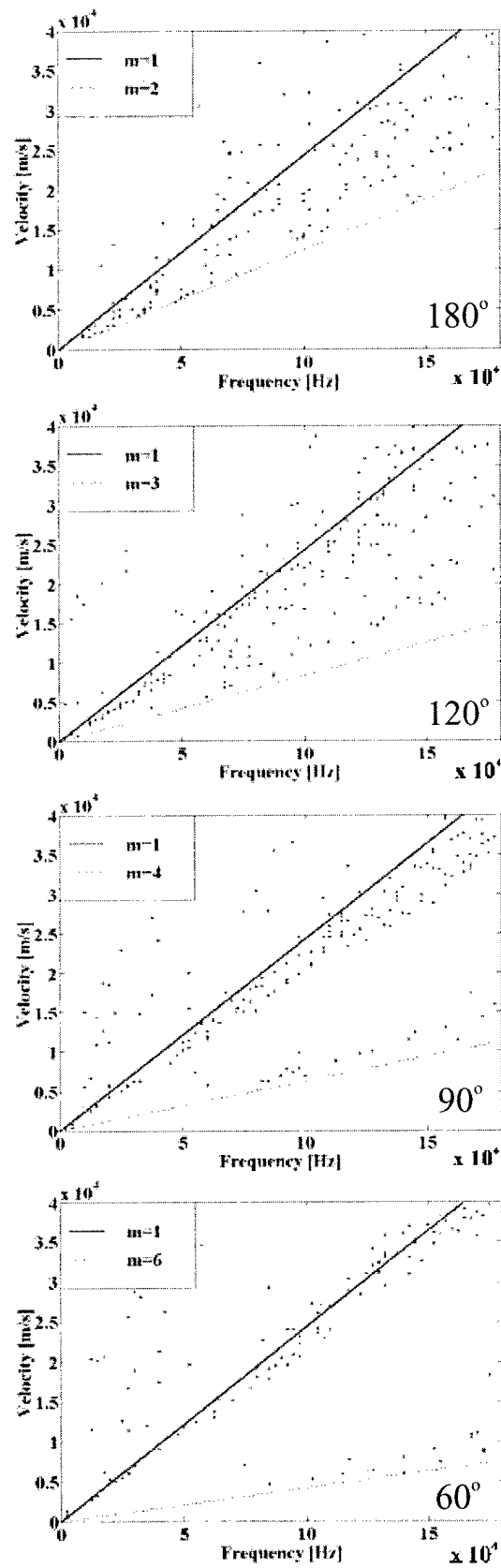


Figure 12. Chesta et al.

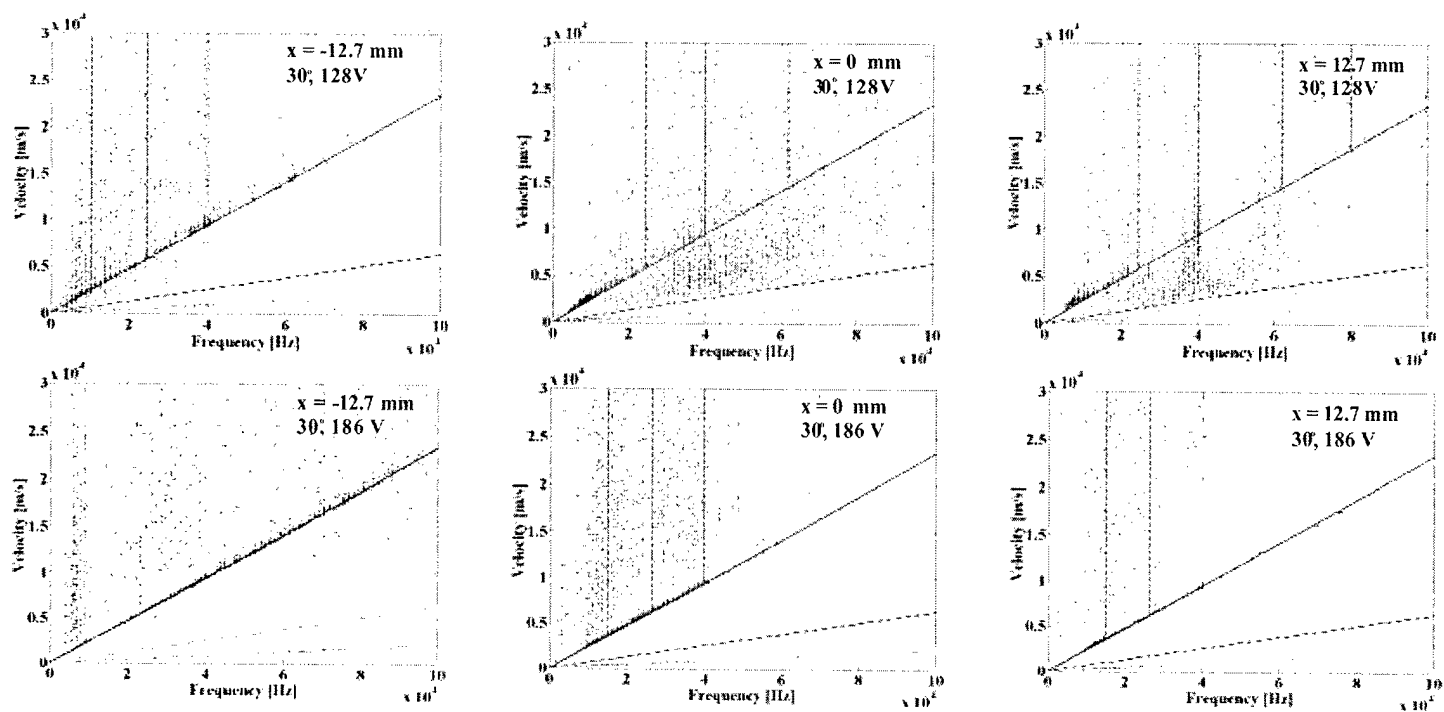


Figure 13. Chesta et al.

Appendix III

Laser-Induced Fluorescence Characteristics of a Helium Arcjet Flow

Q.E. Walker and M.A. Cappelli

To appear in *Applied Optics*, 2001

Laser-Induced Fluorescence characteristics of a helium arcjet flow

Q.E. Walker and M.A. Cappelli

Thermosciences Division, Mechanical Engineering Stanford University

Stanford, CA 94305-3032

Abstract

Laser-Induced Fluorescence is used to measure the velocity and temperature at the exit plane of a low-power helium arcjet. Two cases were examined, one in which the mass flow rate was changed at a constant current, and the other where the current was changed at a constant mass flow rate. At constant mass flow rate, the velocity scales with the increase in power. At constant current, a higher specific energy results in an unexpected lower mean exit velocity. The temperature profiles show that the nozzle wall temperature is greater than the mean exit temperature. Along the axis of the arcjet, these measurements indicate the presence of a shock less than one nozzle diameter downstream of the exit.

Introduction

Arcjet technology is currently in use for north-south stationkeeping on telecommunication satellites. A broader use of arcjets as enabling technologies for space propulsion will require improvements in thrust efficiency or an extension in specific impulse. Both of these will require a better understanding of the physics of arcjet thruster flows. Improved numerical simulations of the arcjet thruster will benefit the development of arcjet designs that achieve extended performance; however, experimental data are needed to verify such flow models. At present, models have evolved to the point where they can treat the magnetohydrodynamic flow and the finite-rate propellant chemistry, but comparisons with experimental data for flows comprised of relatively simple chemistries, such as with molecular hydrogen propellant, continue to show discrepancies between the models and experimental measurements [1,2]. It is difficult to isolate the source for these discrepancies, and to determine if further refinement is needed in the modeling of the propellant chemistry or in the modeling of the arcjet physics. For the majority of propellants, these may be strongly coupled.

In an attempt to make further progress on the understanding of these complex plasma devices, we proposed to extensively study a flow that does not have the difficulties associated with

complex chemical processes. Next to hydrogen, inert gas arcjet flows are more desirable as test beds for model development.

Of the inert gases, helium appears to be the most interesting propellant. It seems to have the highest thrust efficiency (because of its low mass) of any potential arcjet propellant considered for space propulsion use [3]. Because it has the highest ionization energy, is relatively inert, and lacks internal vibrational and rotational energy modes, a higher percentage of the energy deposited into the flow may end up as thrust. Helium cold flow thrusters are currently used for attitude control on many satellites. A compact and efficient low-power helium arcjet would be able to fulfill that role as well.

The goal of this ongoing research project is to characterize the flow structure and properties of helium arcjet thrusters. This paper presents laser-induced fluorescence (LIF) measurements of the velocity and temperature at the exit plane and in the plume of a prototype arcjet thruster. LIF diagnostics has proven to be a robust diagnostic for arcjet flowfields [4,5,6]. The 728.1 nm transition ($2^1P - 3^1S$) is used here for this study because it is well isolated from other transitions and readily accessible with common narrow-band tunable continuous laser sources. A broad range of arcjet operating conditions was examined. The operating conditions were selected to cover a range of specific energies (arcjet power/mass flow rate), by either operating at a set current of 15.0 while the mass flow rate was varied, or by operating at a set mass flow rate of 27 mg/s while the current was varied. The specific energy of the flow determines the specific impulse, and optimum conditions may exist for thrust efficiency and specific impulse as a result of variations in the method in which the arc attaches at the anode within the nozzle.

Experimental Setup

The experimental setup is shown schematically in Fig. 1. The fluorescence excitation laser radiation centered around the 728 nm wavelength is generated by a Coherent 899-21 Ti:Sapphire Ring Laser, pumped by a Nd:YAG Verdi diode laser. The ring-laser power level reached 40 mW with a pump laser power of 5 W. Spectral scanning of the ring-laser was accomplished with the laser scanning electronics which provided control over the piezoelectrically driven intracavity etalon. The maximum scanning range is 20 GHz or approximately 0.035 nm at a wavelength of 728 nm. The laser electronics provides continuous smooth scanning over 20 GHz through optical feedback. According to the laser specifications, the maximum laser linewidth is 20 MHz, which is

established by the frequency jitter. No attempt to independently characterize the linewidth was made in this study.

The output of the Ti:Sapphire ring laser is focused by a single 750 mm focal length achromat lens into the plume of the arcjet. For axial velocity component measurements, optical access to the vacuum chamber is through a 76 mm diameter quartz window on the endplate, aligned axially with the arcjet. A Gaussian beam waist of 50 μ m at the focal plane is determined from the laser output characteristics and properties of the focusing optics. A fraction (10 %) of the laser beam was split off and sent to a Burleigh WV-1000 wavemeter to monitor the laser wavelength, and a Thorlabs Model PDA50 photodiode detector to monitor the laser intensity. In addition, the ring laser intensity was also monitored by a photodiode detector built into the laser head and was independently recorded by the laser-control electronics.

For radial velocity component measurements, a 50 mm diameter sapphire window mounted on the side of the chamber provided optical access along a direction perpendicular to the arcjet axis. Collection and focusing of the fluorescence signal is performed with a combination of a 400 mm focal length plano-convex lens and a 115 mm focal length achromat lens. The fluorescence is focused onto a 200 μ m diameter pinhole, which was used as a field stop or spatial filter. The transverse magnification of 3.3 was determined by the position of the collection lenses, and this resulted in a spatial resolution along the arcjet axial direction of approximately 0.66 mm. The laser beam waist of 50 μ m determines the resolution in the transverse direction.

Immediately after the field stop is a Hamamatsu R928 photomultiplier tube (PMT) operating at a cathode supply of 900 volts. It is enclosed in a light-tight housing with a 10 nm bandwidth interference filter centered about 730 nm mounted on the entrance. The PMT output current is detected as a voltage across a 15 kilohm terminating shunt resistor. Since the fluorescence signal is considerably smaller than the background emission, phase-sensitive detection of the fluorescence was performed with a Stanford Research Systems SR850 digital lock-in amplifier. The excitation laser beam is mechanically chopped at a frequency of 1.5 kHz to provide a reference frequency for the model SR850 and a second, model SR530 lock-in amplifier. The Stanford Research Systems SR530 analog lock-in amplifier is used to measure the photodiode signal which is needed to correct the LIF signal for changes in the laser power during the scan time. The time constant on both lock-in amplifiers was varied from 300 ms, when taking measurements

near the arcjet axis, to 3 s when taking measurements at locations near the periphery of the arcjet nozzle and plume. The arcjet voltage and wavemeter output are also recorded during the scan.

The arcjet used in these experiments is a 1-kW class radiation-cooled laboratory model thruster which was designed and built at the NASA Lewis Research Center. Specific details about the materials and dimensions were reported previously [5]. The vacuum facility consists of a 1.09m x 0.56m diameter stainless-steel chamber pumped by two mechanical pumps and two 1250 CFM blowers through a 15 cm diameter steel pipe. The backpressure was between 18 - 44 Pa during arcjet operation. The arcjet is mounted on translation stages with two degrees of freedom. The measurements at the exit plane were taken by translating the arcjet parallel to excitation laser beam. The axial measurements were taken by moving the arcjet along the axis of the excitation beam. It is noteworthy that this arcjet used in these experiments was originally used as a prototype thruster to understand operation on hydrogen and hydrazine propellants, which experience relatively minor voltage fluctuations. When operating on helium at a given current and mass flow rate, there are more significant fluctuations in the arc voltage. These fluctuations lead to a slightly unsteady flow and therefore a flow with temporal fluctuations in velocity (and temperature). In this study, we report on measurements made while averaging the fluorescence over timescales longer than the period of these fluctuations(~ 1 msec). Fluctuations in velocity will have a "broadening" effect on the fluorescence excitation scans, and will also distort the inferred mean velocity field in a way that is not yet well understood. The inferred temperature should therefore be interpreted as an upper limit on the actual temperature field.

Analysis

A typical LIF scan is shown in Fig. 2. The recorded fluorescence signal from the lock-in amplifier is normalized by the photodiode output to account for variations in laser power during each scan. The laser scan width varied from 15 to 20 GHz with the larger scan widths needed when probing the edges of the flowfield.

The properties of the flowfield are captured in the spectral lineshape. Each scan was fit by a Gaussian to determine the linecenter and full-width at half maximum (FWHM) of the lineshape. The plasma velocity, u , is linearly related to the linecenter shift, $\Delta\lambda$, from a reference wavelength, λ_o , according to the Doppler shift equation

$$\frac{u}{c} = \frac{\Delta\lambda}{\lambda_o} \quad (1)$$

where c is the speed of light in the medium, which in this case can be taken as the speed of light in vacuum. The stationary reference wavelength was obtained by measuring the radial velocity along the centerline of the arcjet at the exit plane. The translational temperature of atomic helium is related to the Gaussian FWHM according to the Doppler broadening equation

$$\Delta_G^{FWHM} = \lambda_0 \sqrt{\frac{8 \ln 2 k T}{m c^2}} \quad (2)$$

where m is the atomic mass of helium and k is Boltzmann's constant.

There are other broadening mechanisms, which can affect the lineshape. We chose experimental conditions that minimized the effects of these broadening mechanisms. One mechanism is power broadening, i.e., the perturbation of the population of atomic states by the laser interaction itself. The induced absorption reduces the number of atoms in the lower ($n=2$) state while increasing the number in the upper ($n=3$) state. If the perturbation of the states involved in the probe transition is small, then the fluorescence signal is linear with laser intensity. When the laser intensity becomes too large, the transition is saturated, and the ratio of populations of the two states approaches the ratio of the state degeneracies. Under these conditions, the fluorescence signal is no longer linear with laser intensity and the resulting spectral excitation lineshape is broadened. We performed a study of the LIF signal response as a function of the laser power. At the typical laser power levels used, 10-40 mW at 728.163 nm, the fluorescence signal is in the linear regime, consistent with simple estimates of the required saturation intensities. Other broadening mechanisms include pressure broadening (both resonance and van der Vall's broadening) and Stark broadening (due to free electrons and ions); however, at the operating static pressures ($p < 1$ Torr) and at the estimated maximum charged particle densities ($\sim 10^{13} \text{ cm}^{-3}$) in these flows these broadening mechanisms are found to be negligible compared to Doppler broadening.

Results

Profiles of the velocity and temperature of the arcjet flowfield were taken near the exit plane and along the centerline under the operating conditions listed in Table 1. As mentioned earlier, two cases were examined, (i) the comparison between different specific energies at a constant current and (ii) the comparison between different power levels at a constant mass flow rate.

Measurements performed at the exit plane did not extend over the entire diameter of the nozzle because of interference due to laser scattering from the nozzle wall. Error bars have been omitted from the velocity profiles to avoid cluttering the figures. The uncertainty in the velocity

measurements are ± 0.40 km/s due largely to uncertainties in the absolute wavelength reading from the wavemeter. For these studies a zero velocity standard was not used. Instead we relied on the radial velocity measurements near the arcjet centerline to provide a zero-velocity estimate. This estimate of the unshifted (zero-velocity) line center wavelength was consistent with tabulated data on the unshifted wavelength for this transition. The error bars for the temperature measurements were omitted for the same reason. Assuming that the line-shape fit is the limiting factor in determining the temperature, the error is based on the noise in the measured fluorescence scan. Near the centerline the typical uncertainty is $\pm 10\%$, and it will approximately double near the periphery of the nozzle.

Exit Plane Measurements

The velocity profiles measured on helium are generally similar in shape to those measured for the same arcjet operating on hydrogen [4,5]. Figure 3 shows the variation in the axial component in the exit-plane velocity with specific energy. In this dataset the mass flow rate was decreased at a constant current of 15A to obtain a higher specific energy. The decrease in velocity with increase in specific energy is somewhat unexpected and implies that the additional energy added to the arcjet is not specifically added to the propellant. As shown in Table 1, the voltage decreased with the decrease in mass flow rate. This decrease in voltage is interpreted as an abrupt transition in the mode of arc attachment, with the arc attaching further upstream in a higher pressure region of the flow. We speculate that in this "low voltage mode" a larger fraction of the energy is deposited in the anode. Figure 4 shows the variation in velocity as the power is changed at a fixed (and relatively high) mass flow rate of 27 mg/sec. It is apparent that at these operating conditions, there is an increase in velocity with increasing specific energy. This trend is expected and has been observed in detailed studies of hydrogen arcjet flows [7]. In nominal hydrogen arcjet flow conditions, the arc is believed to attach in a diffuse mode on the anode, well upstream of the throat of the nozzle. These results demonstrate that specific energy is not necessarily the best metric for achieving higher specific impulse, especially when operating on propellants that have a tendency of being bi-stable in their operating mode of arc attachment.

Figure 5 summarizes the exit plane measurements of velocity for all the specific energies studied. This figure illustrates the results of a similarity analysis that neglects viscous effects in the nozzle

flow, and appropriately groups the variables to plot the non-dimensional velocity versus non-dimensional radius:

$$\frac{u}{\sqrt{P/\dot{m}}} = \frac{r}{r_o} \quad (3)$$

Here, u is the axial velocity, P is the power, \dot{m} is the mass flow rate, r is the radial position, and r_o is the nozzle radius.

The collapse of the data for the constant mass flow case indicates that the flow physics is consistent between the two cases shown, and furthermore, that the viscosity may not be important in characterizing this nozzle flow. It is noteworthy that a similar analysis for a hydrogen arcjet flow did not result in such a collapse of the data [8]. While we do not expect viscous effects to play a more important role at lower mass flow rates, the lack of a collapse in the case of changing mass flow rate for a fixed current suggests a change between conditions in the way that the added energy is lost to other modes including heat transfer to the anode, supporting a possible transition to "low voltage" arc attachment mode. The exit plane temperature profiles are shown in Figs. 6 and 7. Two trends are apparent in these figures. The first is that there is an inverted U-shape describing the variation in temperature across the nozzle, a result that is not seen in hydrogen or simulated hydrazine flows [9]. The second is that the centerline temperatures are not strongly affected by changes in specific energy, however, the temperatures closer to the nozzle wall increase with increases in specific energy. The characteristic U shape in the temperature profiles implies that the fluid expands to a temperature lower than the wall temperature. It suggests that heat transfer from the wall is largely responsible for the inverted profile and that conduction along the nozzle from the upstream region of the arcjet will greatly affect the properties of the nozzle flow. The increase near wall temperature with increased specific energy is consistent with increased energy deposition in the anode in "low voltage" mode.

It is noteworthy that the centerline temperatures are also lower than those seen in either hydrogen or simulated hydrazine flows [7]. At a specific energy of 102 MJ/kg, (1.4 kW and 13.7 mg/s flow rate) the centerline hydrogen temperature is 2000 K [7]. All else being equal, the specific energy of 102 MJ/kg of hydrogen should result in the arcjet flow properties as a specific energy of 51 MJ/kg of helium since the energy deposited on a per molecule basis is approximately equal. However, helium is expected to have a more efficiency conversion of enthalpy to kinetic energy than a hydrogen arcjet since helium has fewer internal energy modes. The higher temperatures measured in hydrogen reflect the added energy in these internal modes, which acts as

a reservoir that eventually drains into translational motion. Previous measurements of high thrust efficiencies in helium arcjets support these arguments [3,10].

Axial Measurements

Figures 8 and 9 show the axial variation in velocity and temperature taken for different specific energies. For the low specific energy (high mass flow rate), the axial velocity is found to be nearly constant within one nozzle radius ($\sim 2\text{mm}$) downstream of the exit plane, while the temperature is found to drop slightly. Beyond this axial location, we see a slight drop in velocity together with an apparent rise in temperature, suggesting the presence of a shock feature. The results are less clear for the high specific energy (low mass flow rate) of the two cases shown. For this later case, the velocity is lower, and the temperature higher than that of the former, again indicating that the mode of operation is less efficient. Also, while the presence of a shock is seen in the axial temperature variation, it is less apparent in the velocity data.

The shock feature is located near the tail of the measured flow pattern, less than one nozzle diameter away from the exit plane. A similar structure was observed in the hydrogen arcjet, and, when operating on Argon, diamond shock patterns are clearly visible with the eye, from the visible plasma emission [4,11]. However, it is emphasized that these results represent time-averaged measurements of the velocity and temperature, making the interpretation of the observed downstream structure still somewhat tenuous. A more extensive study of the near-exit flowfield using impact pressure and mass flux probes is planned for future experiments.

Summary

Laser-induced fluorescence measurements were taken at the exit plane and downstream of the exit plane for a helium arcjet. Velocities and temperatures were measured for two cases, (i) constant current and decreasing mass flow rate, and (ii) constant mass flow rate and decreasing current. These measurements demonstrate quite clearly that simply increasing the specific energy does not necessarily result in greater velocities and therefore greater specific impulse. We found that decreasing the mass flow rate can change the mode of arc attachment and also the fraction of energy that is lost to the anode. The importance of anode heat transfer is seen as inverted U shape temperature profile indicating that the helium plasma expands to temperatures below that of the nozzle. Fluctuations have been seen in the arcjet voltage for all cases studied. These fluctuations will cause the reported temperatures to be higher than actual mean temperature of the flow.

Measurements of velocity and temperature made along the axial direction downstream of the exit plane indicate the presence of a shock in the flowfield, similar to what has been seen in hydrogen arcjet studies. Future experiments will attempt to clarify the external and possibly internal flowfield structure of these helium arcjet flows.

Acknowledgments

This work was supported in part by the Air Force Office of Scientific Research. Partial support for Quentin Walker was provided through a Sloan Foundation Grant. The authors are grateful to NASA Lewis for supplying the arcjet thruster used in these studies.

References

1. Boyd, I., "Extensive Validation of a Monte Carlo Model for Hydrogen Arcjet Flowfields," J. of Propulsion and Power, **13**, 775--782, (1995).
2. Butler, G., Boyd, I., and Cappelli, M., "Nonequilibrium Flow Phenomenon in Low Power Hydrogen Arcjets," AIAA 95-2819, 31st Joint Propulsion Conference, 1995.
3. Welle, R., Pollard, J., Janson, S., Crofton, M., and Cohen, R., "One Kilowatt Hydrogen and Helium Arcjet Performance," The Aerospace Corporation, 1993.
4. Liebskind, J., Temperature and Velocity Diagnostic for an Arcjet Plume using Laser-Induced Fluorescence, Ph.D. thesis, Stanford University, 1994.
5. Storm, P. and Cappelli, M., "Fluorescence Velocity Measurements in the Interior of a Hydrogen Arcjet Nozzle," AIAA Journal, **34**, 853--855, (1996).
6. Liebskind, J., Hanson, R., and Cappelli, M., "Experimental Investigation of Velocity Slip near an Arcjet Exit Plane," AIAA Journal, **33**, 373--375, (1994).
7. Storm, P. and Cappelli, M., "LIF Characterization of Arcjet Nozzle Flows," AIAA-96-2987, 32nd Joint Propulsion Conference, 1996.
8. Storm, P., Optical Investigations of Plasma Properties in the Interior of Arcjet Thrusters, Ph.D. Thesis, Stanford University, 1997.
9. Storm, P. and Cappelli, M., "Stark Broadening Corrections to Laser-Induced Fluorescence Temperature Measurements in a Hydrogen Arcjet Plume," Applied Optics, **35**, 4913--4918, (1996).
10. Walker, Q., Hargus, Jr., W., and Cappelli, M., "Characterization of a Low-Power Helium Arcjet," AIAA-98-3636, 34th Joint Propulsion Conference, 1998.
11. W.A. Hargus, J. and Cappelli, M., "The Structure of an Expanding Hydrogen Arcjet Plasma," Physics of Plasmas, **5**, 4488--4497, (1998).

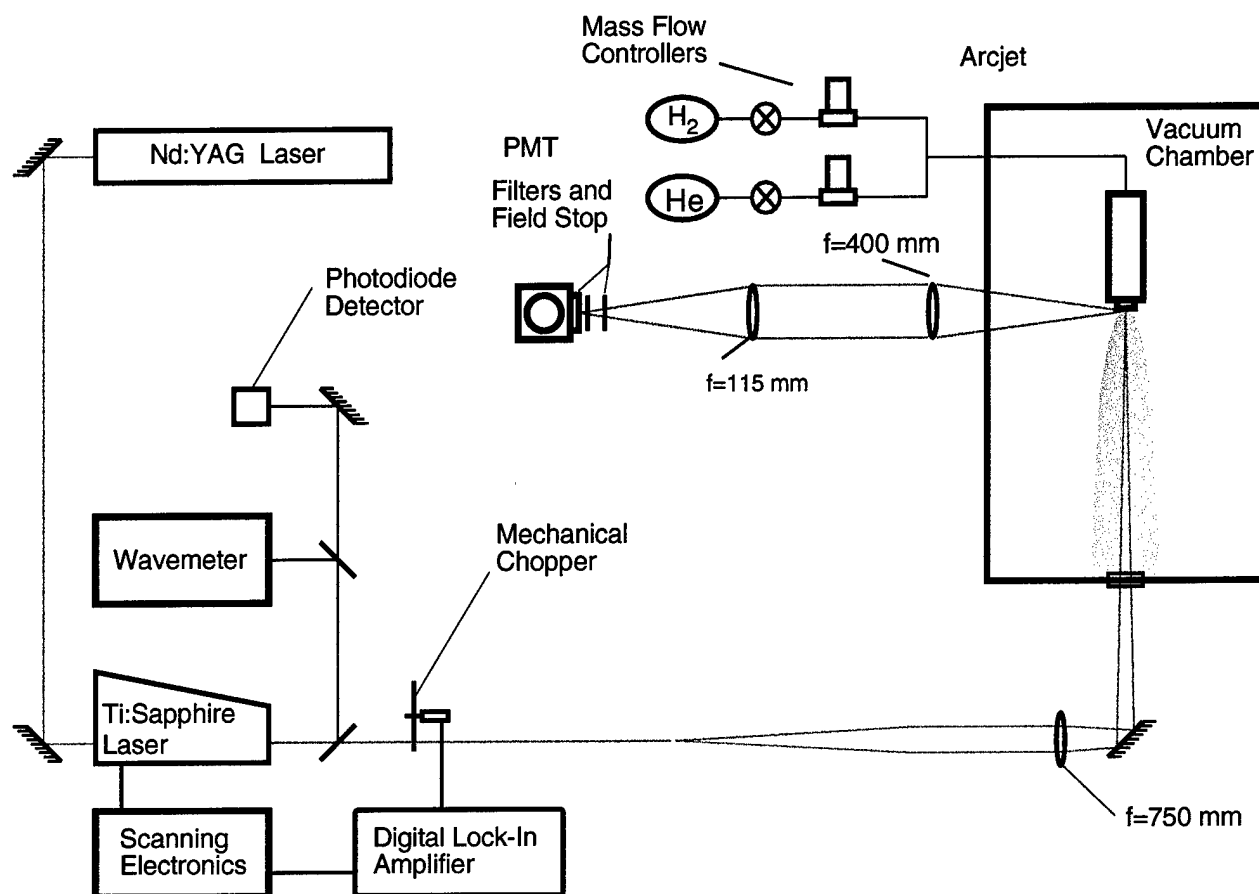


Figure 1. Laser-Induced Fluorescence Experimental Setup

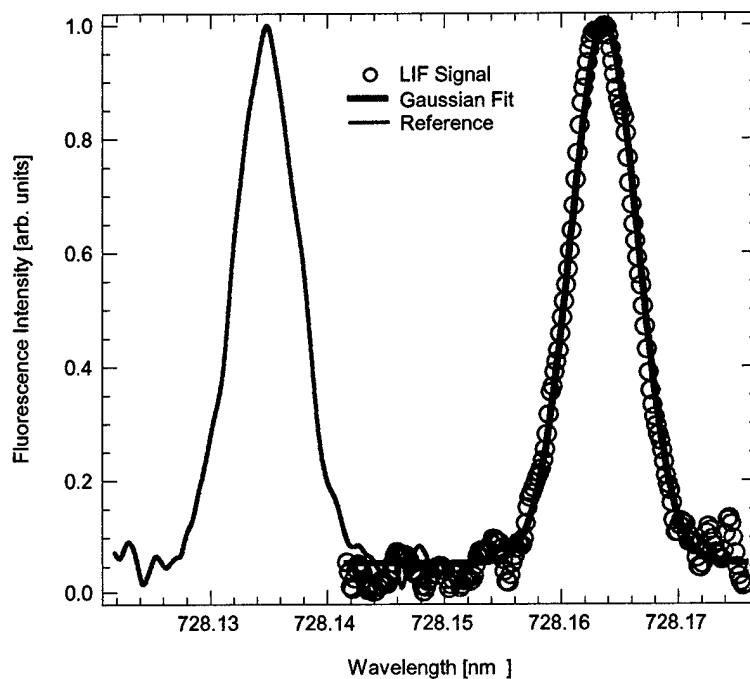


Figure 2. Example Laser-Induced Fluorescence Scan

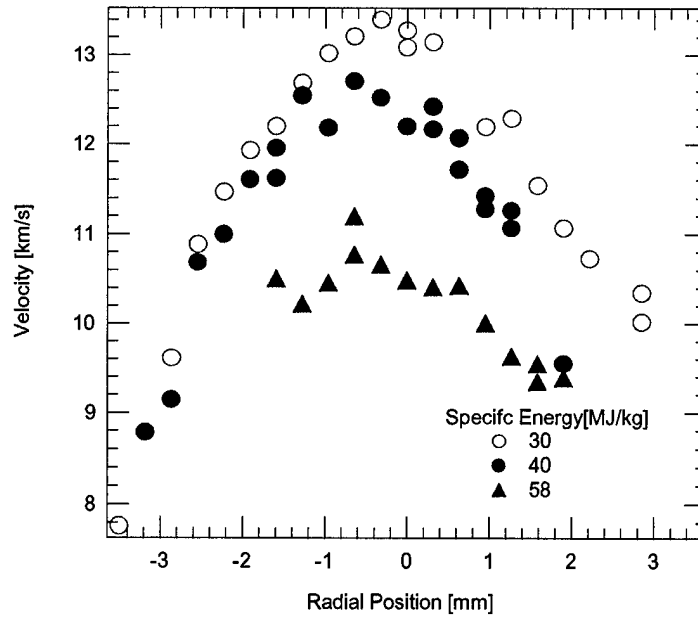


Figure 3. Axial Velocities at the Exit Plane at different Specific Energies

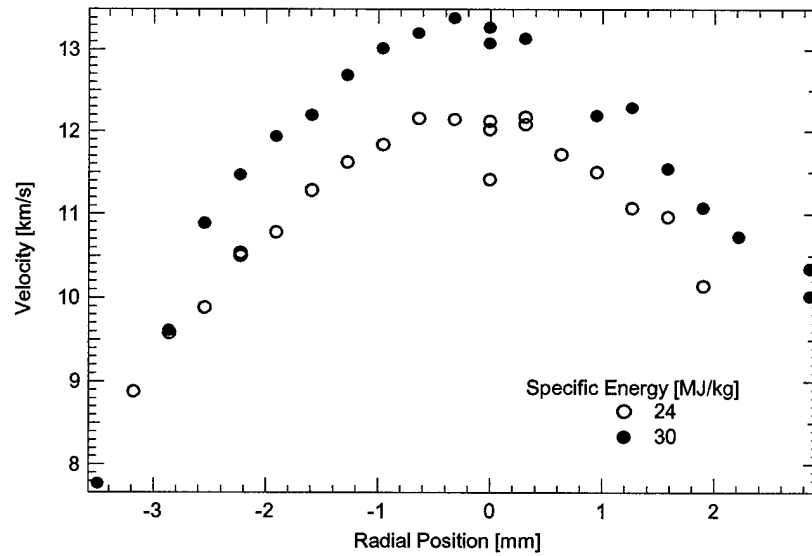


Figure 4. Axial Velocities at the Exit Plane for a Fixed Mass Flow Rate of 27.0 mg/s

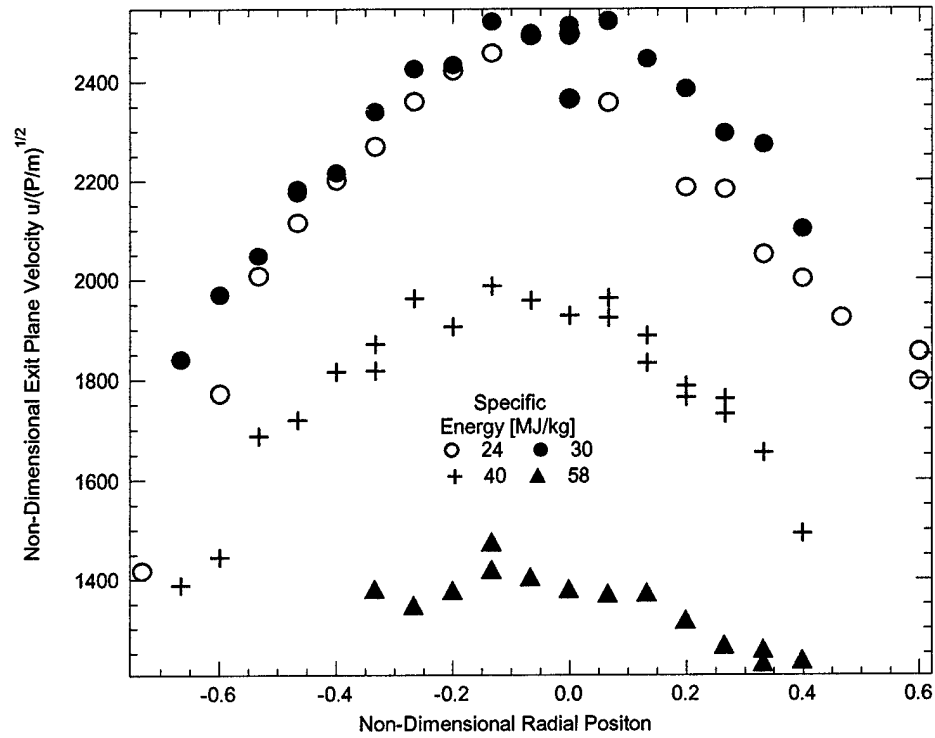


Figure 5. Non-Dimensional Exit Plane Velocities

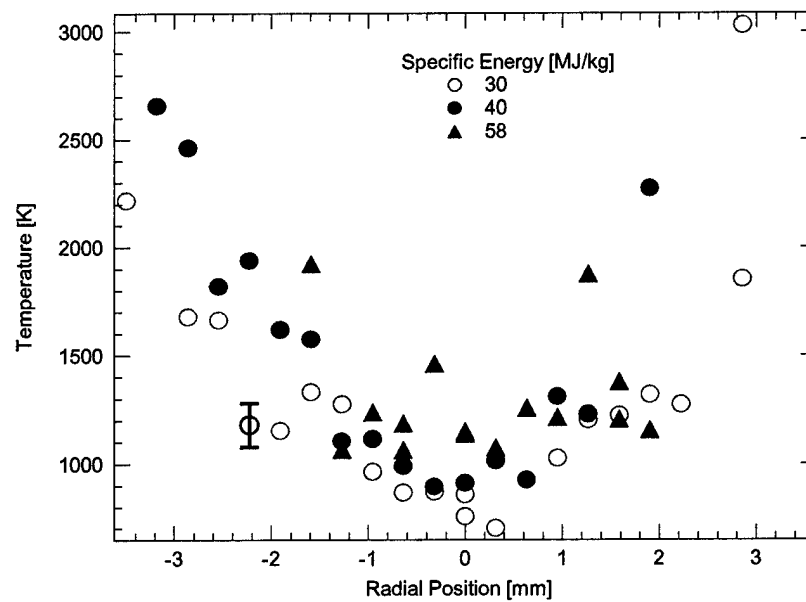


Figure 6. Radial Temperature Profile at the Exit Plane at Different Specific Energies

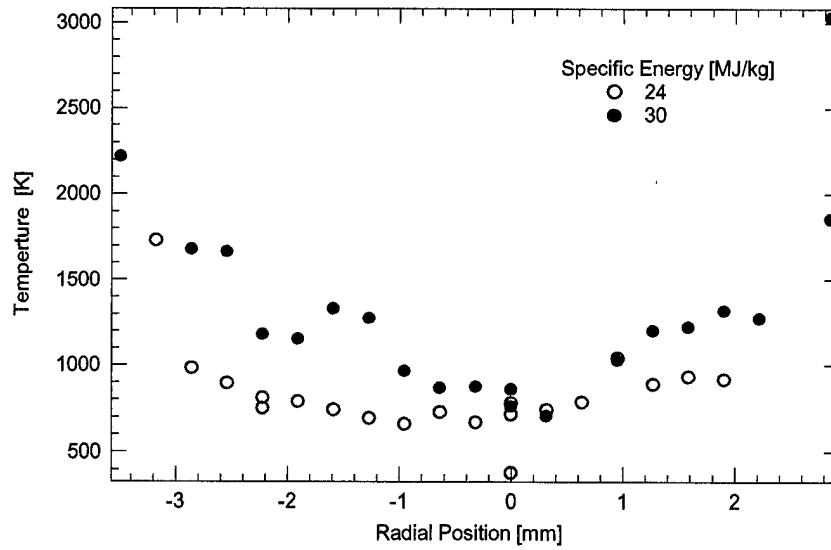


Figure 7. Radial Temperature Profile at the Exit Plane for a Fixed Mass Flow Rate

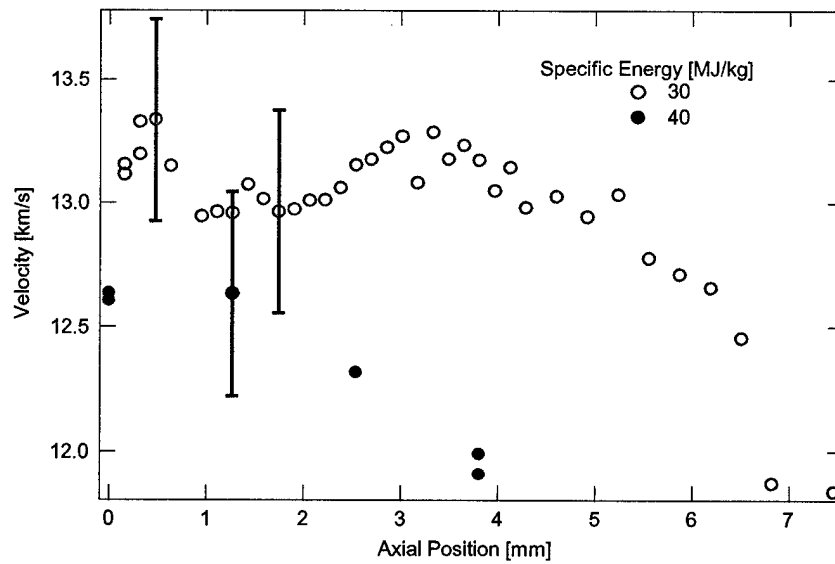


Figure 8. Axial Velocity Profile at Different Specific Energies

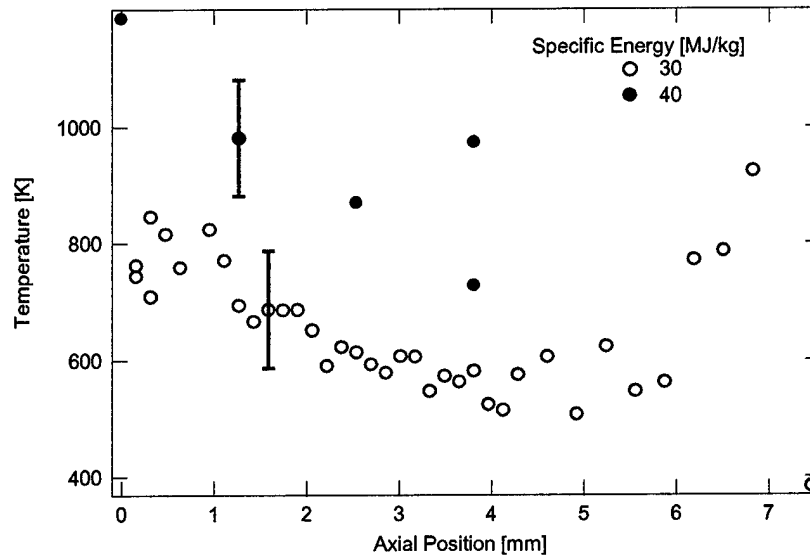


Figure 9. Axial Temperature Profile at Different Specific Energies

Mass Flow Rate [mg/s]	Voltage [V]	Specific Energy [MJ/kg]
27.0	51-57	30
18.0	48-49	40
9.0	35	58
27.0	63	24

Table 1. Helium Arcjet Operating Conditions